SEDIMENTOLOGY the journal of the International Association of Sedimentologists

Sedimentology (2018) **65**, 123–150 doi: 10.1111/sed.12427

Basin-scale thermal and fluid flow histories revealed by carbonate clumped isotopes (Δ_{47}) – Middle Jurassic carbonates of the Paris Basin depocentre

XAVIER MANGENOT*†, MARTA GASPARRINI*, VIRGILE ROUCHON* and MAGALI BONIFACIE†

**IFP Energies Nouvelles, 1-4 avenue de Bois-Préau, Rueil-Malmaison 92852, France (E-mail: xavier-mangenot@club.fr)*

†Institut de Physique du Globe de Paris, Sorbonne Paris Cité, Université Paris Diderot, UMR 7154, CNRS, Paris 75005, France

Associate Editor – Tracy Frank

ABSTRACT

The reconstruction of past diagenetic conditions in sedimentary basins is often under-constrained. This results from both the analytical challenge of performing the required analyses on the minute sample amounts available from diagenetic mineral phases and the lack of tracers for some of the diagenetic parameters. The carbonate clumped isotope thermometry (Δ_{47}) opens new perspectives for unravelling the temperatures of diagenetic phases together with the source of their parent fluids, two parameters that are otherwise impossible to constrain in the absence of exploitable fluid inclusions. Here is reported the study of a large number of sedimentary and diagenetic carbonate phases (from Middle Jurassic reservoirs of the Paris Basin depocentre) by combining detailed petrographic observations with a large number of Δ_{47} data ($n > 45$) on a well-documented paragenetic sequence, including calcite and dolomite burial cements. The data reveal carbonate crystallization at temperatures between 29°C and 98°C from fluids with $\delta^{18}O_{water}$ values between −7‰ and +2‰, in response to the progressive burial and uplift of the Paris Basin, throughout 165 Myr of basin evolution. Coupled with the time–temperature evolution previously estimated from thermal maturity modelling, these temperatures allow determining the timing of four successive cementation episodes. The overall data set indicates a history of complex water mixing with a significant contribution of hypersaline waters from the Triassic aquifers migrated upward along faults during the Cretaceous subsidence of the basin. Subsequent large-scale infiltrations of meteoric waters induced a dilution of these pre-existing brines in response to the Paris Basin uplift in the Tertiary. Overall, the data presented here allow proposing an integrated approach to characterize the cementation events affecting the studied carbonate reservoir units, based on temperature, oxygen isotope composition and salinity of the parent fluids as well as on petrographic grounds.

Keywords Carbonate diagenesis, fluid salinity, fluid flows, Paris Basin, thermal history, Δ_{47} thermometry.

INTRODUCTION

Much of the current knowledge on the thermal, fluid flow and diagenetic histories of sedimentary basins is based on data acquired on rocks and minerals, by means of a variety of tools (Tucker & Wright, 1990; Moore, 2001). In basins, including carbonate successions, the main approach to investigate the thermal and chemical conditions of ancient diagenetic fluids is to examine their fossil archives, by means of the chemical and isotopic compositions of diagenetic minerals and their fluid inclusions (Morse & Mckenzie, 1990; Goldstein & Reynolds, 1994). In particular, the fluid inclusion microthermometry (leading to both temperature and salinity estimates) and the oxygen isotope compositions of carbonates ($\delta^{18}O_{carb}$ – informing on either temperature or the oxygen isotope composition of the parent fluid $\delta^{18}O_{water}$) are widely used for carbonate successions. These methods are well-established and have been largely applied to many carbonate diagenesis case studies, in different geological contexts (Tucker & Wright, 1990; Moore, 2001). Nevertheless, some drawbacks may limit their successful application on carbonate minerals. Indeed, fluid inclusions in carbonate phases are not always present or may not be large enough to be reliably analysed. In addition, post-entrapment processes such as stretching, leakage and refill can also affect the reliability of fluid inclusion microthermometry. On the other hand, the application of the $\delta^{18}O_{carb}$ thermometer requires that the oxygen isotope composition of the parent fluid ($\delta^{18}O_{water}$) from which the mineral formed is known (McCrea, 1950; Epstein *et al.*, 1951). In most cases, $\delta^{18}O_{water}$ values are under-constrained and strong assumptions are needed because the direct measurements of $\delta^{18}O_{water}$ of palaeofluids are difficult to determine on a systematic basis (for example, via isotopic composition of O and/or H in crushed fluid inclusions; Affolter *et al.*, 2014).

The precise and independent estimations of both the absolute precipitation temperature and the $\delta^{18}O_{water}$ composition of the carbonate parent fluid can now be acquired from a single method, carbonate clumped isotope (denoted as Δ_{47}) thermometry (Eiler, 2007), thus overcoming the main limitations of the more conventional techniques. The Δ_{47} thermometry is based on the thermally dependent preference of the heavy isotopes of carbon and oxygen ^{13}C and ^{18}O to bond with one another in the carbonate lattice at low temperatures. It can be applied to various carbonate minerals (for example, calcite and dolomite) and in a wide range of growth temperatures (0 to 300°C; Kluge *et al.*, 2015; Bonifacie *et al.*, 2017). The Δ_{47} thermometry has been applied to a broad array of studies, mainly focused on the reconstruction of Earth surface palaeotemperatures (Passey *et al.*, 2010; Snell *et al.*, 2013) with only few applications to subsurface problems, such as burial and structural diagenesis, water and hydrocarbon fluid flows, and basin thermal evolution (Bristow *et al.*, 2011; Huntington *et al.*, 2011; Loyd *et al.*, 2012, 2015; Budd *et al.*, 2013; Dale *et al.*, 2014; Huntington & Lechler, 2015; Swart *et al.*, 2016).

The aim of this study was to evaluate the contribution of the Δ_{47} tool to the reconstruction of a complete paragenetic sequence, including multiple cement phases with different mineralogy, precipitation temperatures and parent fluid composition, and for which available thermal and fluid flow histories are relatively well-established. For this purpose, the Middle Jurassic subsurface carbonate reservoirs of the central part of the Paris Basin are an ideal geological target, mainly because:

1 They host multiple petrographically well-differentiated carbonate phases (i.e. sedimentary biogenic and abiogenic, different burial diagenetic cements) (Worden & Matray, 1995; Gaumet, 1997)

2 They belong to a stratigraphic succession for which the geodynamic evolution (Guillocheau *et al.*, 2000), formation water geochemistry (Worden & Matray, 1995) and burial histories (Uriarte, 1997) have been studied extensively.

3 The Δ_{47} thermometry and fluid inclusion microthermometry acquired on diagenetic carbonates from the same rock unit (five calcitic or dolomitic cement specimens) show very consistent results (Mangenot *et al.*, 2017), allowing the Δ_{47} data to be confidently used as a solid palaeotemperature (and palaeo-$\delta^{18}O_{water}$) proxy for this study.

This study includes detailed petrographic observations (including ultraviolet light and cathodoluminescence microscopy) and isotopic analyses ($\delta^{18}O$, $\delta^{13}C$ and Δ_{47}) of several samples of bioclasts, micritic matrix and four different calcitic and dolomitic burial cements. All samples were collected from four different Middle Jurassic cores located tens of kilometres apart in the central part of the Paris Basin. After examining the consistency of the petrographic and

isotopic data set, which revealed the thermal and palaeofluid composition of each carbonate phase with unprecedented precision, this study discusses the significance of Δ_{47} for guiding geological interpretations in light of the extended knowledge pre-existing for the Paris Basin.

GEOLOGICAL AND HYDROLOGICAL CONTEXT

The Paris Basin is one of the most documented sedimentary basins in the world. It has been studied since the 18th Century (Guettard, 1746) and is considered a typical example of an intracratonic basin (Brunet & Le Pichon, 1982; Pomerol, 1989; Perrodon & Zabek, 1991). It is mainly composed of Mesozoic sediments lying unconformably on a Palaeozoic basement (Perrodon & Zabek, 1991; Guillocheau *et al.*, 2000). It has been widely studied as an exploration target for oil and gas, hydrological resource, nuclear waste disposal and potential gas storage (natural gas and CO_2). The sedimentary column is *ca* 3000 m thick in the central part of the basin and includes various lithologies spanning from Upper Triassic to Tertiary (Fig. 1A and B). Besides minor uplifts expressed by corresponding unconformities, the Paris Basin experienced a simple burial history punctuated by periods of rapid subsidence in the Jurassic and Late Cretaceous, followed by a major uplift of variable extent during Tertiary tectonism. The four major unconformities have ages corresponding to the Jurassic–Cretaceous transition (late Cimmerian phase); the Late Aptian (Austrian phase); and the Late Cretaceous to Early Tertiary (Guillocheau *et al.*, 2000). These unconformities have been associated with the early stage of the rise of the thermal dome in the central North Sea, a further stage of Atlantic Ocean opening during the Early Cretaceous and Aptian, and Africa–Europe convergence during the Late Cretaceous and Early Palaeogene (Ziegler, 1990). Within the central part of the Paris Basin, these tectonic events led to major compressive flexure and fault reactivation (Fig. 1C). Recent apatite fission track analyses in the southern margin of the Paris Basin revealed that the main tectonic inversion occurred at the Cretaceous–Palaeogene boundary and led to the main uplift phase causing the erosion of 200 to 700 m of Late Cretaceous chalk (Barbarand *et al.*, 2013). The last main tectonic event is related to the Late Eocene to Early Oligocene east–west extension, occurring in the eastern part of the basin (Rhine Graben opening), whereas a compressive regime was dominant in the western part (Guillocheau *et al.*, 2000; André *et al.*, 2010).

The Middle Jurassic carbonates extend across the entire Paris Basin, from exposed outcrops in the eastern and southern margins up to and beyond the English Channel (Purser, 1989; Javaux, 1992; Gaumet *et al.*, 1996; Gaumet, 1997; Delmas *et al.*, 2002). In the depocentre area, the Middle Jurassic carbonates are documented oil and geothermal water reservoirs, which have experienced a complex and still debated hydrogeological history (Fontes & Matray, 1993; Matray *et al.*, 1994; Worden & Matray, 1995). The present-day temperature of the Middle Jurassic strata in the central part of the basin is around 60 to 80°C (Ménétrier *et al.*, 2005; Garibaldi, 2010). However, organic maturity data from Lower Jurassic (mainly Hettangian and Toarcian) shales (Fig. 1F) as well as fluid inclusion and clay mineral thermometric data from Middle Jurassic rocks of the depocentre consistently indicate that they have experienced higher burial temperatures, up to 80 to 100°C (Espitalie *et al.*, 1988; Guilhaumou & Gaulier, 1991; Gaulier & Burrus, 1994; Clauer *et al.*, 1995; Worden & Matray, 1995; Spötl, 1996; Gonçalvès *et al.*, 2010).

The other main reservoirs in the central part of the Paris Basin are the Carnian Chaunoy and the Rhaetian fluvial sandstone units, here grouped together and referred to as the Upper Triassic reservoirs. A Triassic (Keuper) halite body sits to the east and is separated from the Upper Triassic reservoirs by interbedded sands and anhydrite-rich mudstones (Worden *et al.*, 1999). Sandwiched between the Upper Triassic sandstone reservoirs and the Middle Jurassic carbonate reservoirs are Lower Jurassic Hettangian and Toarcian shales, which represent the main source rocks within the basin (Poulet & Espitalie, 1987; Espitalie *et al.*, 1988). The Lower Jurassic source rocks of the Paris Basin only experienced oil window temperatures (90 to 115°C) for the Toarcian shales (Ménétrier *et al.*, 2005). Hydrocarbon maturation started during the Early Cretaceous and reached peak generation at the beginning of the Late Cretaceous (90 to 70 Ma; Monticone *et al.*, 2011). Oil migration possibly started just after, although the main migration seems to have occurred in the Oligocene during an east–west extensional phase (Tremolières, 1981).

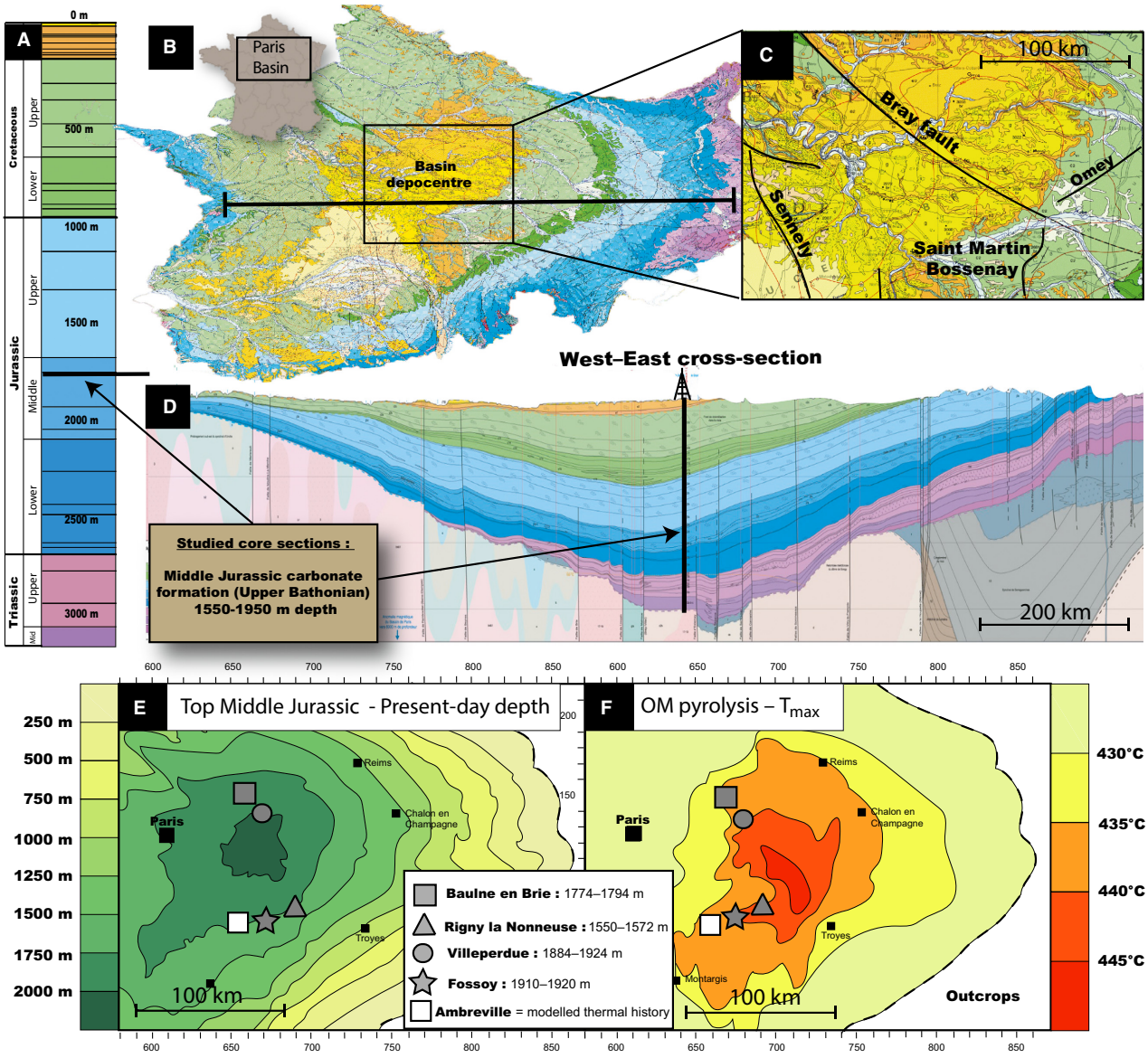

Fig. 1. (A) Synthetic stratigraphic column of the Paris Basin with location of the studied stratigraphic interval (Middle Jurassic carbonates). (B) Geological map of the Paris Basin with location (black frame) of the studied depocentral area (modified after Chantraine *et al.*, 1996). (C) Major faults affecting the studied area (compiled from Guillocheau *et al.*, 2000. (D) West–east geological cross-section of the Paris Basin (modified after Gely & Hanot, 2014) with location of the synthetic stratigraphic column shown in (A). (E) Map of the present-day burial depth at the top of the Middle Jurassic carbonates (modified after Delmas *et al.*, 2002). (F) Map of Rock-Eval T_{max} from pyrolysis of organic matter (OM) of the Lower Toarcian source rocks (modified after Delmas *et al.*, 2002). In (E) and (F), the location of the studied reservoirs is shown with grey dots, whereas the white square represents a well used for thermal history modelling (Uriarte, 1997).

SAMPLES AND METHODS

Sample location and sampling procedure

Four subsurface rock cores were selected from the depocentre of the Paris Basin, corresponding to the following exploration and production wells (present depth of 1500 to 1900 m): Baulne en Brie, Rigny la Nonneuse, Villeperdue and Fossoy. The studied core intervals belong to the same Middle Jurassic lithostratigraphic unit (carbonates of the *Comblanchian Formation*, Upper Bathonian), and consists of similar sedimentary facies (see details in the *Petrographic analysis*

section below). Location of the cores, present-day burial depth of the Middle Jurassic sampled intervals and T_{max} values (from Rock-Eval pyrolysis) of the underlying Lower Jurassic shales are reported in Fig. 1. The studied area covers more than 5000 km^2. A total of 70 rock samples was collected from the four cores to create thin sections (30 μm thick) for petrographic analysis. Geochemical analyses were accomplished on different carbonate phases, manually sampled with a dental drill from the highly polished rock slabs used for the preparation of thin section. A total of 46 samples from both sedimentary and diagenetic carbonates (39 cements of calcite or dolomite, three bioclasts and four micrites) were selected and drilled for isotopic analyses.

Petrographic analysis

All of the prepared thin sections were carefully analysed using conventional transmitted light and cathodoluminescence microscopy (CL). This was essential to select homogeneous specimens, and avoid phase mixing during manual sampling, prior to geochemical analysis. The CL apparatus used in the study was a Nikon Eclipse ME600 microscope (Nikon Instruments Inc., Tokyo, Japan) equipped with a CITL Mk5 (CITL Analytical instruments, Welwyn, UK) connected to an OPEA system (Cathodyne OPEA, 16–20 kV with a 420–660 μA beam current; Optique Electronique, Fontenay, France). In order to detect fluorescence, thin sections were observed under ultraviolet (UV) light, via a Nikon Eclipse LV 100 POL microscope (Nikon Instruments Inc.) equipped with a mercury vapour lamp (100 W). Porosity types, calcite cement habits and dolomite textures were described using the classifications from Choquet & Pray (1970), Flugel (2004) and Sibley & Gregg (1987), respectively.

Δ_{47}, $\delta^{18}O$ and $\delta^{13}C$ measurements and data processing

Measurements of Δ_{47}, $\delta^{18}O$ and $\delta^{13}C$ compositions of carbonate samples were performed at Institut de Physique du Globe de Paris (IPGP, Stable Isotope Team) with a Thermo Scientific MAT253 gas-source mass spectrometer (Thermo Fisher Scientific, Waltham, MA, USA) after digestion of carbonate powder in 104% phosphoric acid. About 5 mg of carbonate was reacted at 90°C in a common acid bath for 20 min for calcites and 1 h for dolomites. The methods used for carbonate digestion, CO_2 purification and isotope measurements follow the procedure detailed in Bonifacie *et al.* (2017). Each measurement consisted of 70 cycles of comparison between the CO_2 extracted from the sample against a working internal reference CO_2 gas [Oztech; with $\delta^{13}C = -3{\cdot}72‰$ and $\delta^{18}O = -6{\cdot}06‰$, versus VPDB (Vienna Pee Dee Belemnite), verified with the international carbonate reference material NBS19]. The signal integration time was 26 s (i.e. total integration time of 1820 s for each CO_2 sample) for a signal of 12V on m/z = 44. Each carbonate sample was analysed two or three times to determine its Δ_{47}, $\delta^{18}O$ and $\delta^{13}C$ compositions in eight discrete analytical sessions. Traditional $\delta^{18}O$ and $\delta^{13}C$ carbonate compositions were acquired as part of each Δ_{47} analysis, and ^{17}O corrections were made using the parameters from Santrock *et al.* (1985). In order to account for the temperature dependence of oxygen isotope fractionation between CO_2 gas and carbonate, resulting from the reaction with phosphoric acid at 90°C, a fractionation factor of 100 811 for calcite and 10 093 for dolomite was used (following Rosenbaum & Sheppard, 1986; Katz *et al.*, 2017). The $\delta^{18}O$ and $\delta^{13}C$ of the carbonate samples are expressed in ‰ relative to the VPDB standard.

For constructing correction frames for processing raw Δ_{47} values, CO_2 gases driven to isotopologue equilibrium at both 1000°C and 25°C were used. The equilibrated CO_2 gas standards in this study have bulk isotopic compositions spanning the entire range of measured cement samples, were purified and analysed in the same way as carbonate samples or carbonate standards and were typically run every four to five analyses (Table S1). The raw Δ_{47} data were first corrected for linearity effects using a fixed common equilibrated gas line slope fitted to the equilibrated CO_2 gases at both 1000°C and 25°C. Subsequently, as recommended by Dennis *et al.* (2011), the raw Δ_{47} values (expressed relative to the working gas) were transferred into the Carbon Dioxide Equilibrated Scale (CDES) using the CO_2 gases driven to isotopologue equilibrium at both 1000°C and 25°C with theoretically predicted Δ_{47} values of 0·0266‰ and 0·9252‰, respectively (after Wang *et al.*, 2004). Finally, Δ_{47} data were projected into the 25°C acid digestion reference frame for easier comparison with previously published calibration data. For this, an acid fractionation value of +0·092‰, determined by Henkes *et al.* (2013), was added.

To ensure accuracy of the entire data reduction process, and ultimately the accuracy of the Δ_{47}

data presented here, two carbonate reference materials, also reported by Dennis *et al.* (2011) and many other studies, were routinely analysed (IPGP-Carrara marble and 102-GCAZ01b). One of these two carbonate standards was analysed typically every five analyses and distributed along the diagenetic cement samples in all runs, in order to check for analytical stability/accuracy of the whole procedure (including carbonate digestion, CO_2 purification, stability of the conditions for analyses of CO_2 inside the mass spectrometer and/or accuracy of the correction frames constructed with standards of equilibrated CO_2 gas – namely the accuracy of the equilibrated gas lines and empirical transfer function lines), as well as long-term reproducibility of the Δ_{47} measurements. The Δ_{47} values obtained for these carbonate reference materials over the period of this study (July 2014 to December 2015) are as follows: Δ_{47} = 0·413 ± 0·016‰ [1 SD (one standard deviation), n = 34] for IPGP-Carrara and Δ_{47} = 0·719 ± 0·019‰ (1 SD, n = 27) for 102-GC-AZ01b. These Δ_{47} values are indistinguishable from those obtained in previous studies (e.g. Dennis *et al.*, 2011; Henkes *et al.*, 2013) and on a longer timescale at IPGP (Bonifacie *et al.*, 2017). Noticeably, the recent work of Daëron *et al.* (2016) and Schauer *et al.* (2016) underlines that when the ^{17}O parameters from Brand *et al.* (2010) are used to process isotopic data [instead of the ^{17}O parameters from Santrock *et al.* (1985) commonly used in the clumped isotope community to date], small differences in Δ_{47} values may arise, with direction and magnitude depending on the bulk isotopic composition of the samples and of the standards of equilibrated CO_2 gas used to transfer the data into the CDES reference frame. However, it should be noted that such reprocessing only led to small differences in Δ_{47} values of the standards and samples (i.e. less than ±0·010‰), within the analytical reproducibility on Δ_{47} measurements, and thus does not significantly change the reported temperatures (and conclusions) of this study.

Finally, the corrected Δ_{47} values were then converted into temperatures ($T\Delta_{47}$) using the interlaboratory composite Δ_{47}-T calibration recently determined for all carbonate minerals for the 0 to 300°C temperature range [i.e. eq. 3 from Bonifacie *et al.* (2017) that compiles 103 mean Δ_{47} data from seven different laboratories and with proper error propagation – that is Δ_{47} = 0·0422*10^6/T + 0·2182 in the 25°C acid digestion reference frame]. The oxygen isotopic compositions of the water [$\delta^{18}O_{water,}$ expressed relative to VSMOW (Vienna Standard Mean Ocean Water)] from which the carbonates precipitated were calculated for each estimated $T\Delta_{47}$ using the $\delta^{18}O_{carb}$ values measured for the carbonate, as well as the oxygen isotope fractionation between the carbonate and water from O'Neil (1969) for calcites and Horita (2014) for dolomites.

RESULTS

Petrography and paragenesis

The four studied cored intervals correspond to the Upper Bathonian (Middle Jurassic) *Comblanchian Formation* (Purser, 1989; Gaumet *et al.*, 1996; Gaumet, 1997). The reconstructed depositional profile includes, from proximal to distal: (i) a grain-dominated lithoclast-rich intertidal deposit with bird's-eye and fenestral porosities; (ii) a mud-dominated succession deposited within a protected lagoon rich in green algae (*Cayeuxias* and *Dasycladaceas*) and benthic foraminifera (*Meyendorfinas*); and (iii) an open platform deposit rich in crinoids, isolated corals and shell fragments from brachiopods and bivalves. The intertidal to lagoonal facies locally display bird's-eye structures with geopetal infill by internal micritic sediment and calcite spars. The porosity evaluated from petrographic observations is low (<5%) and was modified through time by a broad spectrum of diagenetic processes, including multiple cementation episodes, dissolution, neomorphism, mechanical and chemical compaction and micro-fracturing. In this study, only two brachiopods and one bivalve, with no hints of diagenetic alteration (i.e. showing non-luminescent pristine fibres; see Fig. 2A and B), were used for the geochemical characterization of syn-sedimentary carbonates. Presently, most of the primary and secondary pores are filled by calcite and dolomite cements (Figs 2 to 4). Petrographic relationships between carbonate cements and other diagenetic products allowed the establishment of a complete paragenetic sequence, composed of 14 stages (Fig. 5), ranging from syn-sedimentary to late burial processes in the current study.

A more detailed petrographic study was focused on the five main generations of calcite and dolomite cements, named Cal0, Cal1, Dol1, Cal2 and Dol2. The petrographic features of these cements are illustrated in Figs 2 to 4. Although these cements do not always occur in

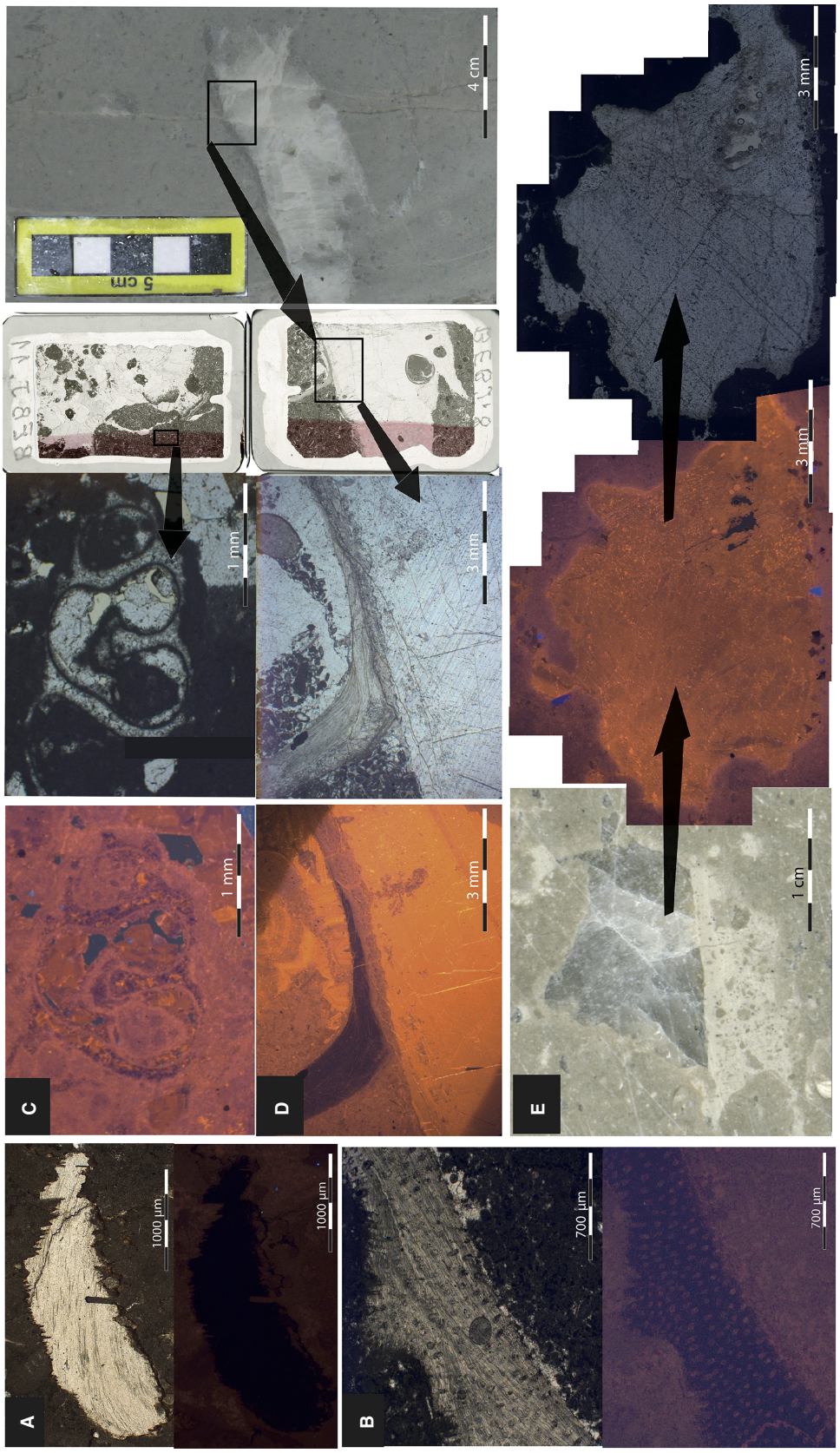

Fig. 2. Macrophotography, thin-section scans and microphotography [transmitted light and cathodoluminescence microscopy (CL)] of the main petrographic features of brachiopods shells, Cal0 and Cal1 blocky calcite cement from the studied Middle Jurassic carbonates. (A) Microphotography (transmitted light and CL) of a fractured and stylolitized unpunctuate non-luminescent brachiopod shell. 1788br sample, Baulne en Brie, 1788 m depth. (B) Microphotography (transmitted light and CL) of a non-luminescent punctuate brachiopod shell. RN 26 sample, Rigny la Nonneuse, 1547 m depth. (C) Microphotograph of a gastropod shell showing the aragonite dissolution process, followed by Cal0 and Cal1 pore-filling cements. BEBJ11 sample, Baulne en Brie, 1790 m depth. (D) Cal1 blocky cement displays a uniform bright orange CL. BEBJ8 sample, Baulne en Brie, 1785 m depth. (E) Cal1 blocky cement displays a uniform bright orange CL. RN23 sample, Rigny la Nonneuse, 1551 m depth.

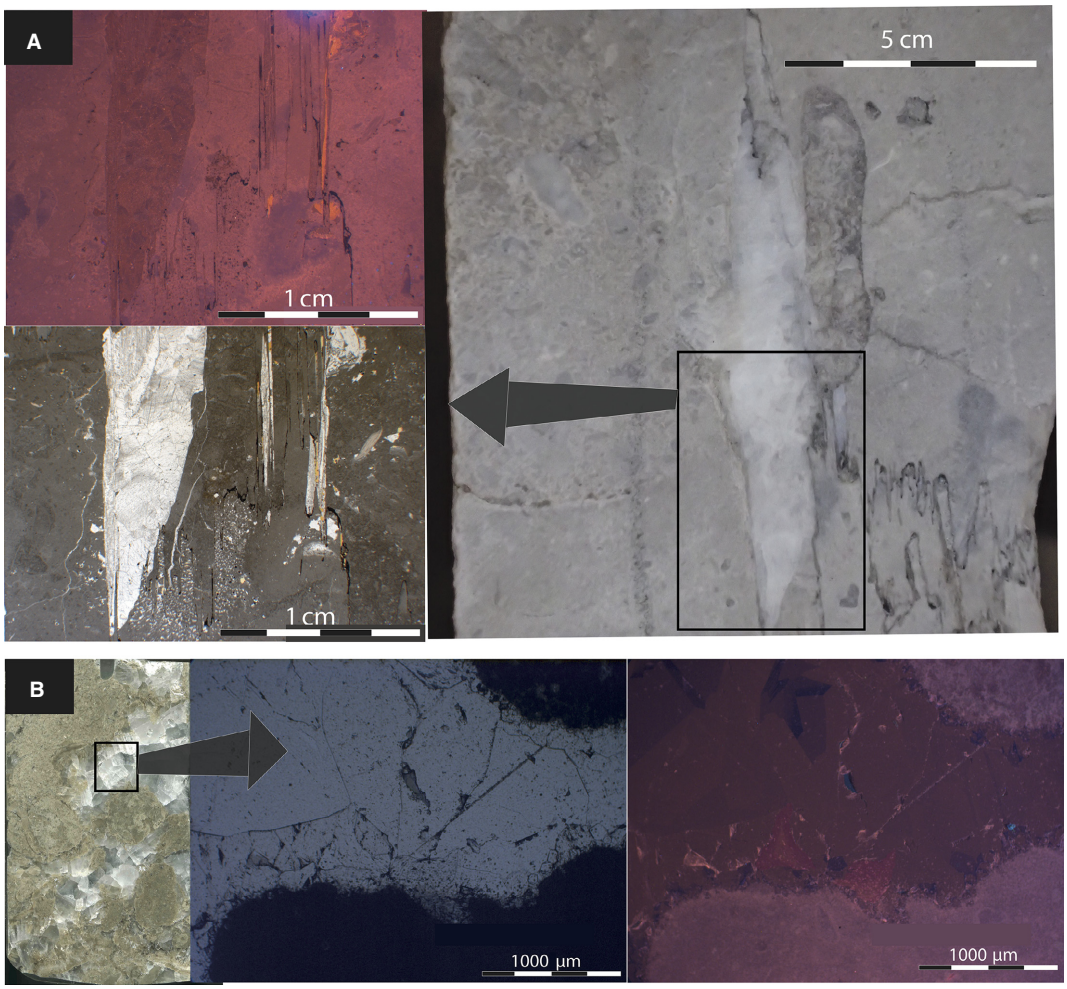

Fig. 3. Macrophotography, thin-section scans and microphotography [transmitted light and cathodoluminescence microscopy (CL)] illustrating the major petrographic features of Cal2 blocky calcite cement. (A) Cal2 cement with uniform dull red to brown CL precipitated in a tension gash. BEBJ2 sample, Baulne en Brie, 1789 m depth. (B) Cal2 cement with a dull red to brown CL, precipitated in large fenestral pores. RN18 sample, Rigny la Nonneuse, 1555 m depth.

each of the four investigated cores, a generalized mineral paragenesis, based on CL cement stratigraphy, was reconstructed (Fig. 5).

The Cal0 cementation event includes two petrographically distinct non-ferroan calcites, lining abiotic grains and fenestral or mouldic pores (Fig. 2C). The former is defined by a rim of non-luminescent bladed calcite crystals (10 to 40 µm) with zoned bright yellow CL. The latter is characterized by a rim of equant granular crystals with a uniform dull brown to red CL. Due to their habit and CL response, these calcite cements possibly precipitated during eogenesis, respectively, from meteoric and marine fluids (as also reported by Tucker & Wright, 1990 and Flugel, 2004). These cements represent a volumetrically minor cementation event and could not be sampled for geochemical analyses.

Fig. 4. Macrophotography, thin-section scans and microphotography [transmitted light, cathodoluminescence microscopy (CL) and ultraviolet (UV) light] of the main petrographic features of Dol1 and Dol2 cements. (A) Vuggy pores partially filled by dull red to brown Cal2 and bright red Dol2 cements. RN3 sample, Rigny la Nonneuse, 1580 m depth. The porosity is highlighted in blue. (B) Pore filled by saddle dolomite (Dol1). Dol1 crystals display curved crystal faces and zoned CL (non-luminescing, with dull red concentric zones). VPU4 sample, Villeperdue, 1921 m depth. (C) Dol1 crystal contains hydrocarbon-bearing fluid inclusions, fluorescing green under UV light. VPU4 sample, Villeperdue, 1921 m depth.

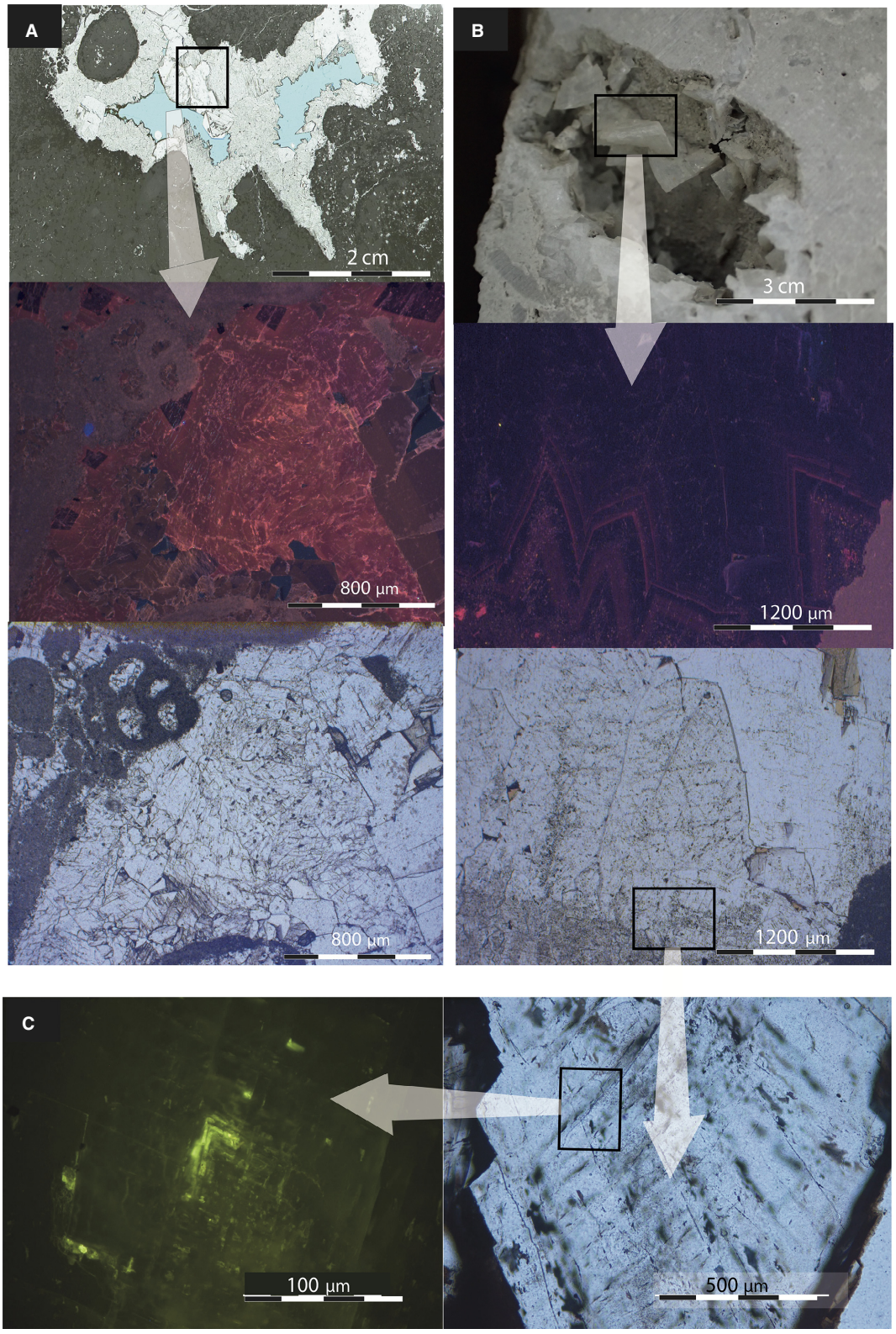
A
2 cm
800 µm
800 µm
B
3 cm
1200 µm
1200 µm
C
100 µm
500 µm

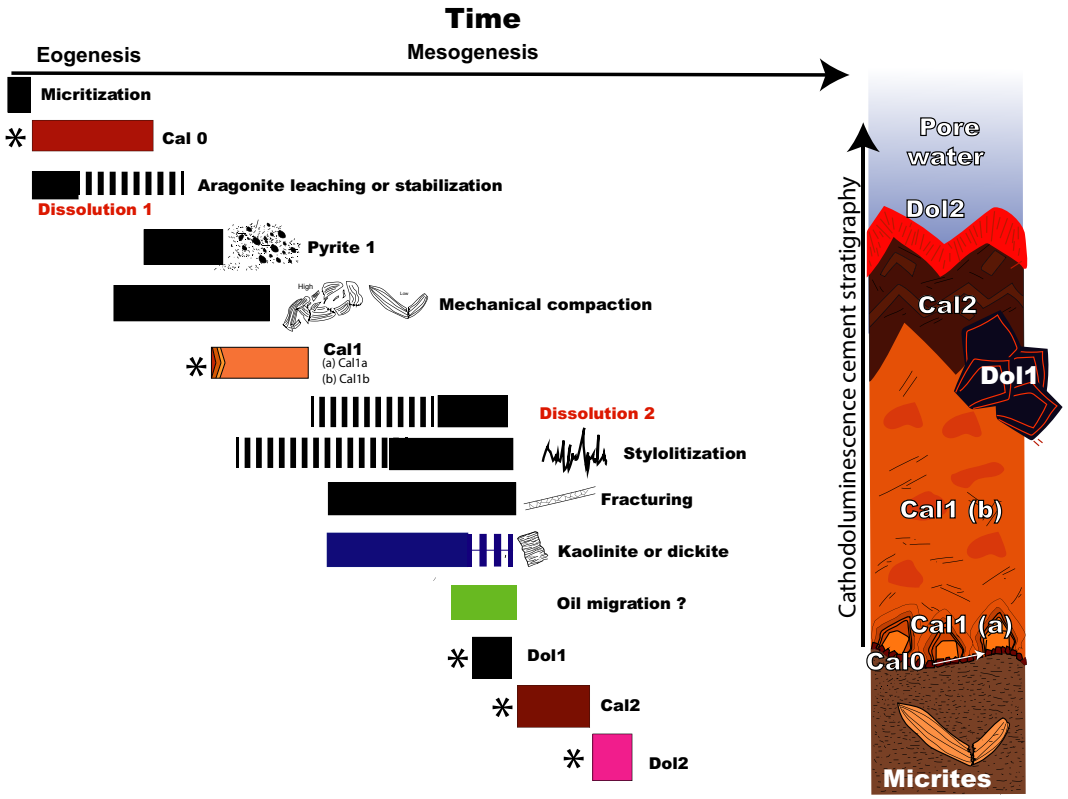

Fig. 5. Paragenetic sequence, composed of 14 diagenetic events, reconstructed for the Middle Jurassic carbonates from the four studied cores (left). A sketch illustrates the succession of the main cementation events and their CL (cathodoluminescence microscopy) response (right). The carbonate phases illustrated in the cement stratigraphy sketch are highlighted by asterisks.

However, they possibly played a role in promoting early induration of the muddy lagoonal sediments that reduced the impact of successive mechanical compaction during burial.

Type Cal1 is composed of blocky crystals of non-ferroan calcite that filled a variety of pore types: interparticle, fenestral, mouldic and vuggy. This cement induced an important reduction of the remaining pore space and seems to be the main cause for the present-day relatively low porosity of the studied carbonate reservoirs. It can be subdivided into two petrographic types, named here, respectively, Cal1(a) and Cal1(b). Type Cal1(a) is rarely observed and consists of crystals (10 to 100 μm) displaying concentric zonation under CL, with bright orange and dull orange zones. In contrast, Cal1(b) is more common and consists of crystals (100 μm to 2 mm) which display a homogeneous bright orange CL (Fig. 2C to E). Type Cal1(b) is referred to simply as Cal1 in the following text, figures and tables, because it is the only petrographic type of Cal1 that could be further investigated with geochemical tools.

Type Dol1 is composed of dolomite crystals (200 μm to 2 mm) which display curved crystal faces (Fig. 4B and C) and an undulose extinction, typical of saddle dolomites (Searl, 1989). The crystals exhibit a concentric zoned CL, dominantly non-luminescent with some thin red zones (Fig. 4B). This dolomite cement is non-ferroan and mostly occurs within fenestral pores, commonly showing geopetal features. Primary hydrocarbon-bearing fluid inclusions were observed in Dol1 crystals (Fig. 4C), in the Villeperdue and Fossoy cores. These inclusions display shapes (rectangular to negative crystal) controlled by crystallographic planes and are assembled along crystal growth zones.

Type Cal2 is composed of non-ferroan blocky calcite crystals (100 μm to 1 mm), mostly precipitated in pore spaces created by diagenetic modifications occurring after Cal1 precipitation (for example, stylolite planes opening, micro-fracturing and partial dissolution of Cal1). The Cal2 cement displays a uniform dull red to brown CL (Fig. 3) with only minor sectorial zoning.

Type Dol2 is composed of saddle dolomite crystals (100 to 500 μm) precipitated as overgrowths on Dol1 with a uniform bright red CL (Fig. 4A). It represents the last carbonate cement of the reconstructed mineral paragenesis. Dol2 cement is rarely observed and never voluminous. Although it was petrographically identified in the four studied cores, it could be sampled for geochemical purposes only from the Rigny la Nonneuse core. Although most of the above-described cements have been petrographically recognized in the four studied cores, they were not always voluminous enough to be sampled for geochemical analyses.

Stable isotope data ($\delta^{18}O_{carb}$, $\delta^{13}C_{carb}$, Δ_{47} and $\delta^{18}O_{water}$)

Table 1 reports the average $\delta^{18}O_{carb}$, $\delta^{13}C_{carb}$, Δ_{47}, $T\Delta_{47}$ and $\delta^{18}O_{water}$ values determined from two to three replicate isotopic measurements of the same powder for each investigated carbonate sample, belonging to six genetically different carbonate phases. Detailed information on each single measurement, correction and standardization can be found in the supplementary material of Appendix S1 (Table S1). Remarkably, each of the six investigated carbonate phases shows a discrete combination of their $\delta^{18}O_{carb}$, $\delta^{13}C_{carb}$, $T\Delta_{47}$ and $\delta^{18}O_{water}$ values with only limited variations among samples of each phase (although the investigated samples are from four different core sections, tens of kilometres apart). Table 2 reports, for each of the six carbonate phases, their average $\delta^{18}O_{carb}$, $\delta^{13}C_{carb}$, Δ_{47}, $T\Delta_{47}$ and $\delta^{18}O_{water}$ values (obtained from two to 21 samples, and that represent a total of three to 51 isotopic measurements for a given carbonate phase) together with their respective 1 SD of the mean.

The carbon isotope compositions of all the different calcite cements (average $\delta^{13}C_{carb} = 1{\cdot}81 \pm 0{\cdot}34‰$, $n = 32$ samples for Cal1 and Cal2; Table 2) fall into the same range as the micrites (average $\delta^{13}C_{carb} = 1{\cdot}75 \pm 0{\cdot}27‰$, $n = 4$ samples) but are significantly lower than for the dolomite cements (average $\delta^{13}C_{carb} = 3{\cdot}2 \pm 0{\cdot}4‰$, $n = 6$ samples for Dol1 and Dol2) (Fig. 6). In contrast, the six discrete carbonate phases investigated show a significant scatter in their oxygen isotope compositions (average $\delta^{18}O_{carb}$ values varying by more than 13‰) although with homogeneous $\delta^{18}O_{carb}$ values when only one carbonate phase is considered (with 1 SD values averaging at ±0·5‰). As such, the average $\delta^{18}O_{carb}$ values are clustered at $\delta^{18}O_{carb} = -1{\cdot}59 \pm 0{\cdot}97‰$ ($n = 3$ samples) for the bioclasts; $\delta^{18}O_{carb} = -4{\cdot}09 \pm 0{\cdot}61‰$ ($n = 4$ samples) for the micrites; $\delta^{18}O_{carb} = -6{\cdot}97 \pm 0{\cdot}72‰$ ($n = 21$ samples) for Cal1; $\delta^{18}O_{carb} = -9{\cdot}23 \pm 0{\cdot}39‰$ ($n = 4$ samples) for Dol1; $\delta^{18}O_{carb} = -15{\cdot}27 \pm 0{\cdot}49‰$ ($n = 11$ samples) for Cal2; and $\delta^{18}O_{carb} = 13{\cdot}50 \pm 0{\cdot}37‰$ ($n = 2$ samples) for Dol2. The $\delta^{18}O_{carb}$ values of the three analysed bioclasts fall within the range of expected values for biogenic calcites, precipitated in equilibrium with Middle Jurassic seawater (Veizer *et al.*, 1999).

Similar to the $\delta^{18}O_{carb}$ values, the different carbonate phases investigated show a significant scatter in their Δ_{47} compositions (i.e. Δ_{47} varying from 0·524 to 0·678‰ in all of the investigated samples), with however very clustered Δ_{47} values when only one carbonate phase is considered (with 1 SD of the mean averaging at ± 0·009‰). Remarkably, each of the six carbonate phases shows a discrete combination of tightly clustered $\delta^{18}O_{carb}$ and Δ_{47} values (Fig. 7). As such, marine bioclasts yield average Δ_{47} values of $0{\cdot}663 \pm 0{\cdot}013‰$ (1 SD; Table 2), corresponding to average temperature of 29 ± 4°C. Samples of the surrounding micrite display strictly lower Δ_{47} values (mean $\Delta_{47} = 0{\cdot}636 \pm 0{\cdot}007‰$, 1 SD), corresponding to significantly higher temperatures of 45 ± 3°C. The other groups correspond to different phases of diagenetic cements with average Δ_{47} values of $0{\cdot}587 \pm 0{\cdot}009‰$ for Cal1, $0{\cdot}537 \pm 0{\cdot}009‰$ for Dol1, $0{\cdot}557 \pm 0{\cdot}008‰$ for Cal2 and $0{\cdot}582 \pm 0{\cdot}007‰$ for Dol2 (with all uncertainties reported as 1 SD with $n = 21$, 4, 9 and 2, respectively). Those very homogeneous Δ_{47} values inside each carbonate phase can be converted into precise temperature estimates, with $T\Delta_{47}$ of 64 ± 4°C for Cal1, 90 ± 6°C for Dol1, 78 ± 4°C for Cal2 and 67 ± 3°C for Dol2 (with all uncertainties reported as 1 SD of the mean). For each investigated carbonate phase, the reported standard deviation of the mean for Δ_{47} data (between 0·007‰ and 0·009‰, typically resulting from a total number of three to 51 analyses depending on the generation studied) is lower than those obtained on homogeneous carbonate standards (with typical 1 SD of ±0·017‰ on $n > 50$ measurements in the present study). This further suggests the high homogeneity of the carbonates investigated here at both the subsample scale and between the different cogenetic cement phases collected in different core sections located tens of kilometres apart.

The oxygen isotopic compositions of the parent fluids for the six carbonate phases investigated exhibit variable values, with respective

Table 1. Stable isotope (Δ_{47}, $\delta^{18}O$ and $\delta^{13}C$) results from individual diagenetic cements.

Sample	Mineralogy	CL behaviour	#*N*	$\delta^{18}O$ ‰, VPDB	$\delta^{13}C$ ‰, VPDB	Δ_{47}* ‰, CDES	$T\Delta_{47}$† °C	$\delta^{18}O_{water}$‡ ‰, VSMOW
Baulne en Brie core								
First generation of block calcite (Cal1 cements)								
BEBJ8	Calcite	Bright orange	3	−7·23 ± 0·03	1·18 ± 0·02	0·586 ± 0·004	66	2·4
BEBJ6	Calcite	Bright orange	3	−5·62 ± 0·14	2·04 ± 0·07	0·592 ± 0·024	63	3·6
BEBJ9	Calcite	Bright orange	2	−6·47 ± 0·08	1·25 ± 0·02	0·572 ± 0·004	72	4·0
BEBJ11	Calcite	Bright orange	3	−6·06 ± 0·04	1·78 ± 0·03	0·588 ± 0·006	65	3·4
BEBJ12	Calcite	Bright orange	3	−5·84 ± 0·05	1·65 ± 0·02	0·596 ± 0·010	61	3·0
BEBJ21	Calcite	Bright orange	2	−6·95 ± 0·01	0·9 ± 0·01	0·593 ± 0·025	63	2·2
BEBJ13	Calcite	Bright orange	2	−7·06 ± 0·03	1·04 ± 0·03	0·593 ± 0·004	63	2·1
BEBJ5	Calcite	Bright orange	2	−5·86 ± 0·04	1·66 ± 0·01	0·585 ± 0·018	66	3·7
BEBJ2	Calcite	Bright orange	2	−7·35 ± 0·20	1·70 ± 0·05	0·579 ± 0·013	69	2·7
BEBJ2	Calcite	Bright orange	2	−5·69 ± 0·06	1·45 ± 0·07	0·592 ± 0·011	63	3·5
Second generation of block calcite (Cal2 cements)								
BEBJgeode	Calcite	Dull red-brown	3	−15·26 ± 0·06	1·99 ± 0·17	0·551 ± 0·011	83	−3·5
BEBJ2	Calcite	Dull red-brown	2	−15·15 ± 0·01	1·79 ± 0·18	0·548 ± 0·001	84	−3·3
Micrite								
BEBJ8	Calcite	Dull red	2	−3·82 ± 0·03	1·78 ± 0·04	0·640 ± 0·013	44	2·3
BEBJ2	Calcite	Dull red	2	−4·66 ± 0·01	1·37 ± 0·01	0·628 ± 0·011	49	2·3
BEBJ11	Calcite	Dull red	2	−4·54 ± 0·11	1·89 ± 0·04	0·642 ± 0·019	43	1·4
BEBJ7	Calcite	Dull red	2	−3·35 ± 0·12	1·99 ± 0·07	0·635 ± 0·021	46	3·1
Biogenic calcite								
1788Br	Calcite	Not luminescent	3	−0·66 ± 0·06	2·82 ± 0·21	0·652 ± 0·031	33	3·5
BEBbiv	Calcite	Not luminescent	2	−1·51 ± 0·12	1·79 ± 0·02	0·678 ± 0·016	24	0·8
Rigny la Nonneuse core								
First generation of block calcite (Cal1 cements)								
RN128	Calcite	Bright orange	3	−7·18 ± 0·08	1·75 ± 0·02	0·574 ± 0·014	71	3·1
RN23	Calcite	Bright orange	3	−7·07 ± 0·16	1·76 ± 0·03	0·581 ± 0·010	66	2·5
AP1516	Calcite	Bright orange	2	−7·28 ± 0·12	1·85 ± 0·05	0·579 ± 0·005	69	2·7
AP1517 (2)	Calcite	Bright orange	2	−7·07 ± 0·02	2·00 ± 0·07	0·572 ± 0·030	74	3·6
RN46	Calcite	Bright orange	3	−7·16 ± 0·01	1·95 ± 0·01	0·581 ± 0·013	68	2·7
Second generation of block calcite (Cal2 cements)								
RN18c	Calcite	Dull red-brown	3	−16·30 ± 0·05	1·84 ± 0·03	0·564 ± 0·017	76	−5·4
RN17	Calcite	Dull red-brown	3	−14·92 ± 0·06	2·21 ± 0·01	0·563 ± 0·025	77	−3·9
RN15	Calcite	Dull red-brown	3	−15·40 ± 0·14	2·23 ± 0·06	0·566 ± 0·024	75	−4·7
RN153	Calcite	Dull red-brown	3	−15·99 ± 0·15	1·88 ± 0·05	0·546 ± 0·009	85	−4·0
RN69	Calcite	Dull red-brown	3	−14·97 ± 0·06	2·15 ± 0·02	0·565 ± 0·004	76	−4·1
Rngeode	Calcite	Dull red-brown	2	−15·26 ± 0·01	2·20 ± 0·02	0·553 ± 0·016	82	−3·6
RN4	Calcite	Dull red-brown	2	−15·11 ± 0·07	2·20 ± 0·01	0·561 ± 0·003	78	−4·0
RN10	Calcite	Dull red-brown	2	−15·07 ± 0·04	2·26 ± 0·01	0·566 ± 0·008	75	−4·3
RN7	Calcite	Dull red-brown	2	−14·58 ± 0·11	2·19 ± 0·01	0·569 ± 0·002	74	−4·0
Second generation of saddle dolomite (DOL2)								
Rndol2 (1)	Dolomite	Bright red	2	−13·24 ± 0·15	3·20 ± 0·01	0·578 ± 0·004	70	−6·4
Rndol-2 (2)	Dolomite	Bright red	1	−13·77	3·11	0·587	66	−7·6
Biogenic calcite								
RNbrachio-1	Calcite	Dull red	2	−2·61 ± 0·79	2·14 ± 0·11	0·658 ± 0·004	31	1·1
Fossoy core								
First generation of saddle dolomite (DOL1)								
FOS1608-1	Dolomite	Black	2	−9·33 ± 0·02	3·02 ± 0·02	0·541 ± 0·001	88	0·1
FOS1610-1	Dolomite	Black	3	−9·57 ± 0·05	3·18 ± 0·05	0·524 ± 0·008	98	1·1
FOS1607-1	Dolomite	Black	2	−8·66 ± 0·36	2·86 ± 0·36	0·545 ± 0·002	86	0·5

Table 1. (continued)

Sample	Mineralogy	CL behaviour	#*N*	$\delta^{18}O$ ‰, VPDB	$\delta^{13}C$ ‰, VPDB	Δ_{47}* ‰, CDES	$T\Delta_{47}$† °C	$\delta^{18}O_{water}$‡ ‰, VSMOW
Villeperdue core								
First generation of blocky calcite (Cal1)								
VPU1 -	Calcite	Bright orange	2	−7·74 ± 0·11	1·70 ± 0·01	0·580 ± 0·004	69	2·3
VPU3	Calcite	Bright orange	2	−8·05 ± 0·86	1·88 ± 0·04	0·592 ± 0·017	63	1·1
VPU6	Calcite	Bright orange	2	−7·57 ± 0·04	1·74 ± 0·07	0·594 ± 0·013	63	1·6
VPU7	Calcite	Bright orange	2	−7·45 ± 0·01	1·80 ± 0·03	0·587 ± 0·010	65	2·0
VPU8	Calcite	Bright orange	2	−7·55 ± 0·01	2·06 ± 0·05	0·597 ± 0·015	61	1·3
VPU9	Calcite	Bright orange	3	−7·21 ± 0·03	1·75 ± 0·07	0·600 ± 0·025	60	1·5
VPU9 bis	Calcite	Bright orange	2	−7·80 ± 0·01	1·81 ± 0·01	0·601 ± 0·020	59	0·8
First generation of saddle dolomite (Dol1)								
VPU4	Dolomite	Black	3	−9·39 ± 0·04	3·61 ± 0·03	0·537 ± 0·016	90	0·3

CL is cathodoluminescence microscopy. #*N* is the number of replicate measurements of the same carbonate powder. Uncertainties are reported as one standard deviation (1 SD) of the mean. *Δ_{47} values are relative to the 'carbon dioxide equilibrium scale' CDES, to which have been applied an acid fractionation factor of 0·092‰ (following Henkes *et al.*, 2013). †Palaeotemperatures calculated using the composite Δ_{47}-T calibration (Eq. 3 from Bonifacie *et al.*, 2017). ‡Oxygen isotope compositions of mineralizing waters are calculated using $T\Delta_{47}$ and the equations of fractionation of oxygen isotopes between the carbonate and water of either O'Neil (1969) for calcite and Horita (2014) for dolomite.

Table 2. Average composition for each cement population.

Phase	Mineralogy	CL behaviour	#*n*	$\delta^{18}O$ ‰, VPDB	$\delta^{13}C$ ‰, VPDB	Δ_{47}* ‰, CDES	$T\Delta_{47}$† °C	$\delta^{18}O_{water}$‡ ‰, VSMOW
Synthesis by cement populations								
Biogenic	Calcite	Not luminescent	3 (7)	−1·59 ± 0·97	2·25 ± 0·52	0·663 ± 0·013	29 ± 4	1·8 ± 1·4
Micrite	Calcite	Dull red	4 (8)	−4·09 ± 0·61	1·75 ± 0·27	0·636 ± 0·007	45 ± 3	2·3 ± 0·7
Cal1	Calcite	Bright orange	21 (51)	−6·97 ± 0·72	1·67 ± 0·31	0·587 ± 0·009	64 ± 4	2·5 ± 1·0
Dol1	Dolomite	Black	4 (10)	−9·23 ± 0·39	3·6 ± 0·16	0·537 ± 0·009	90 ± 6	0·5 ± 0·4
Cal2	Calcite	Dull red-brown	11 (28)	−15·27 ± 0·49	2·08 ± 0·17	0·557 ± 0·008	78 ± 4	−4·1 ± 0·5
Dol2	Dolomite	Bright red	2 (3)	−13·50 ± 0·37	3·15 ± 0·06	0·582 ± 0·007	67 ± 3	−7·0 ± 0·8

CL is cathodoluminescence microscopy. #*n* is the number of discrete investigated sample for a single population (the number in parentheses is the total number of isotopic measurements for each population). Uncertainties are reported as one standard deviation (1 SD) of the mean. For *, †, ‡ refer to Table 1.

average $\delta^{18}O_{water}$ and their associated 1 SD of the mean of +1·8 ± 1·4‰ for the bioclasts, +2·3 ± 0·7‰ for the micrites, +2·5 ± 1‰ for Cal1, 0·5 ± 0·4‰ for Dol1, −4·1 ± 0·5‰ for Cal2 and −7·0 ± 0·8‰ for Dol2. As illustrated in Figs 7B and 8, the carbonate parent fluids show slightly positive O isotopic compositions for the syn-sedimentary carbonates (bioclasts and micrites) and Cal1 blocky calcites. The parent fluids then become slightly depleted in ^{18}O going from Cal1, to Dol1 and Cal2, to reach the most negative $\delta^{18}O_{water}$ values for Dol2, which is the last phase of the mineral paragenesis. Because each of the six carbonate phases investigated here is highly homogeneous in its $\delta^{18}O_{carb}$, $\delta^{13}C_{carb}$ and Δ_{47} data, all the $T\Delta_{47}$ and $\delta^{18}O_{water}$ as well as $\delta^{18}O_{carb}$ and $\delta^{13}C_{carb}$ values reported and discussed hereafter are values averaged by phase.

PREVIOUSLY PUBLISHED MICROTHERMOMETRIC DATA

Microthermometry analyses have been accomplished by previous authors (Matray *et al.*, 1989; Demars, 1994; Worden & Matray, 1995; Mangenot *et al.*, 2017) for two-phase aqueous

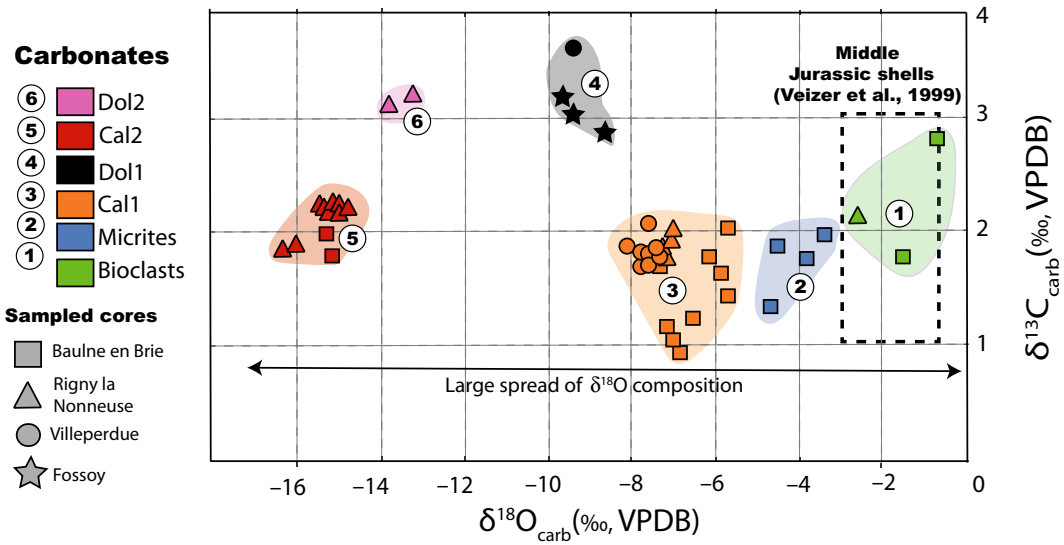

Fig. 6. Stable oxygen and carbon isotope composition of the sedimentary and diagenetic carbonates studied here. The colours of the symbols refer to specific carbonate phases (numbered from '1' to '6'). The shapes of the symbols refer to the cores of provenance. The coloured areas illustrate the dispersion of $\delta^{18}O_{carb}$ and $\delta^{13}C_{carb}$ values for each carbonate phase. Uncertainties are included in the symbol size. The dashed box represents $\delta^{18}O$ and $\delta^{13}C$ values of biogenic calcites precipitated in equilibrium with Middle Jurassic seawater (from Veizer *et al.*, 1999).

fluid inclusions in carbonate cements from the Middle Jurassic carbonates of the Paris Basin depocentre. The results, including homogenization temperatures (Th) and total salinities, are compiled in Fig. 9. These former microthermometry data (from Matray *et al.*, 1989; Demars, 1994; Worden & Matray, 1995) are distinguished from the most recent data (from Mangenot *et al.*, 2017), acquired on five samples from the Baulne en Brie and Fossoy cores. The former authors did not differentiate the various carbonate phases bearing the measured fluid inclusions, thus their microthermometric data probably record the mixing of different generations of fluid inclusions (Fig. 9A.1 and 9B.1). Conversely, prior to microthermometry analysis, Mangenot *et al.* (2017) differentiated three geochemically and petrographically different carbonate phases (transmitted light, UV light and CL), which correspond to Cal1 (two samples), Dol1 (one sample) and Cal2 (two samples) of the present study (Fig. 9A.2 and 9B.2).

Fluid inclusions from undifferentiated cements measured by Matray *et al.* (1989), Demars (1994) and Worden & Matray (1995) display a large range of homogenization temperatures (55 to 120°C), with a broad mode and salinities (0 to 25 wt% NaCl eq), with a multimodal distribution (Fig. 9A.1 and 9B.1). Although the microthermometry data from Mangenot *et al.* (2017) globally overlap those reported from these previous authors, more precision is gained since the three carbonate cements are considered separately (Fig. 9A.2 and 9B.2). Indeed, both homogenization temperatures and salinities, acquired with such petrographic control, are more consistent (Fig. 9A.2 and 9B.2).

Mangenot *et al.* (2017) also evaluated the crystallization temperatures for the same five carbonate samples via clumped isotope (Δ_{47}) analysis. This study reveals a very good consistency between the thermal information acquired from these two independent palaeothermometers. The usefulness of these previous studies for the present survey is two-fold:

1 The high-resolution microthermometry data from Mangenot *et al.* (2017), which globally overlap the data of previous authors on petrographically undifferentiated carbonate cements from several subsurface cores, allow discussion of the diagenetic evolution of the Middle Jurassic reservoirs at a larger scale.

2 The good consistency between the thermal information acquired by fluid inclusion and clumped isotope thermometry on the same samples of Cal1, Dol1 and Cal2 (five samples in total) in the 60 to 100°C temperature range demonstrates the accuracy of the $T\Delta_{47}$ estimates, which were achieved in this study on an additional 35 samples collected from the same carbonate rock unit.

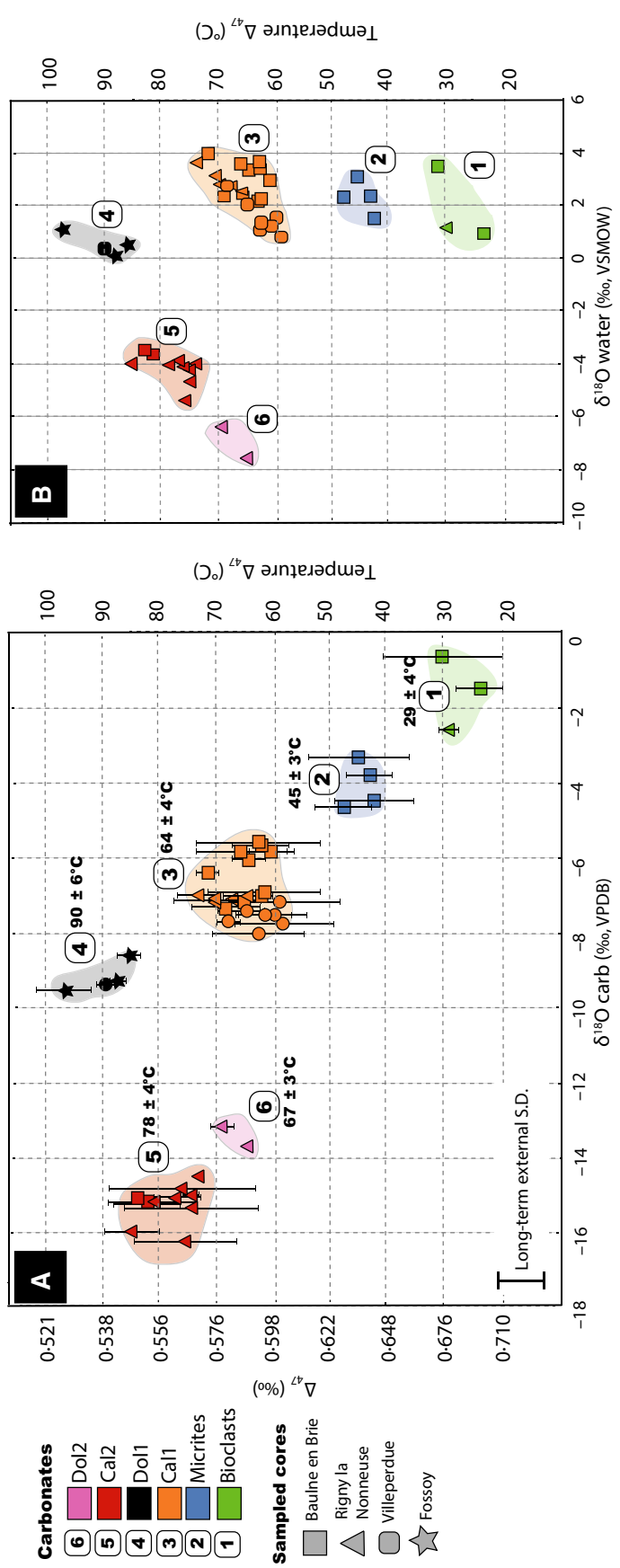

Fig. 7. (A) Cross-plot of the carbonate precipitation temperatures versus conventional $\delta^{18}O_{carb}$ estimated from Δ_{47} thermometry. Reported uncertainties on each data point are one standard deviation (1 SD) of the mean for replicate measurements of the same carbonate powder for TΔ_{47} and are included in the symbol size for $\delta^{18}O_{carb}$ values (Table 1). The long-term external Δ_{47} reproducibility measured on more than 50 carbonate standards over the course of this study (i.e. ±0·017‰) is also reported on the left bottom side for comparison. The six investigated carbonate phases are represented with different colours. Average temperatures calculated from all of the samples of each carbonate phase are also reported in bold with their respective 1 SD of the mean (Table 2). (B) Cross-plot of the carbonate precipitation temperatures estimated from Δ_{47} thermometry versus $\delta^{18}O_{water}$ values back-calculated from Δ_{47} and $\delta^{18}O_{carb}$ compositions.

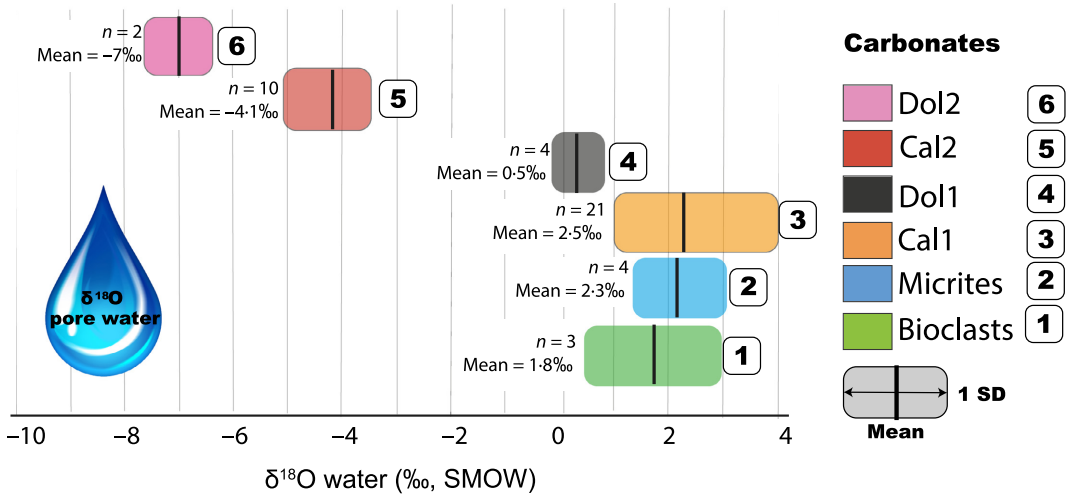

Fig. 8. Average oxygen isotope composition of the carbonate parent fluids ($\delta^{18}O_{water}$) for each investigated carbonate phase (Table 2). The length of the coloured rectangles represents one standard deviation of the mean $\delta^{18}O_{water}$ value calculated for each carbonate phase (reported as vertical black bars and on the left of each box, together with the number of samples considered).

DISCUSSION

Carbonates formed in surface and subsurface settings record the temperature and isotope composition of the fluids from which they precipitated (i.e. the parent fluids). The samples investigated here recorded exceptional petrographic homogeneity and discrete average Δ_{47} values for the six carbonate phases identified. The temperature homogeneity suggests similar burial temperatures characterizing the host rocks at the time of cementation, whereas the compositional

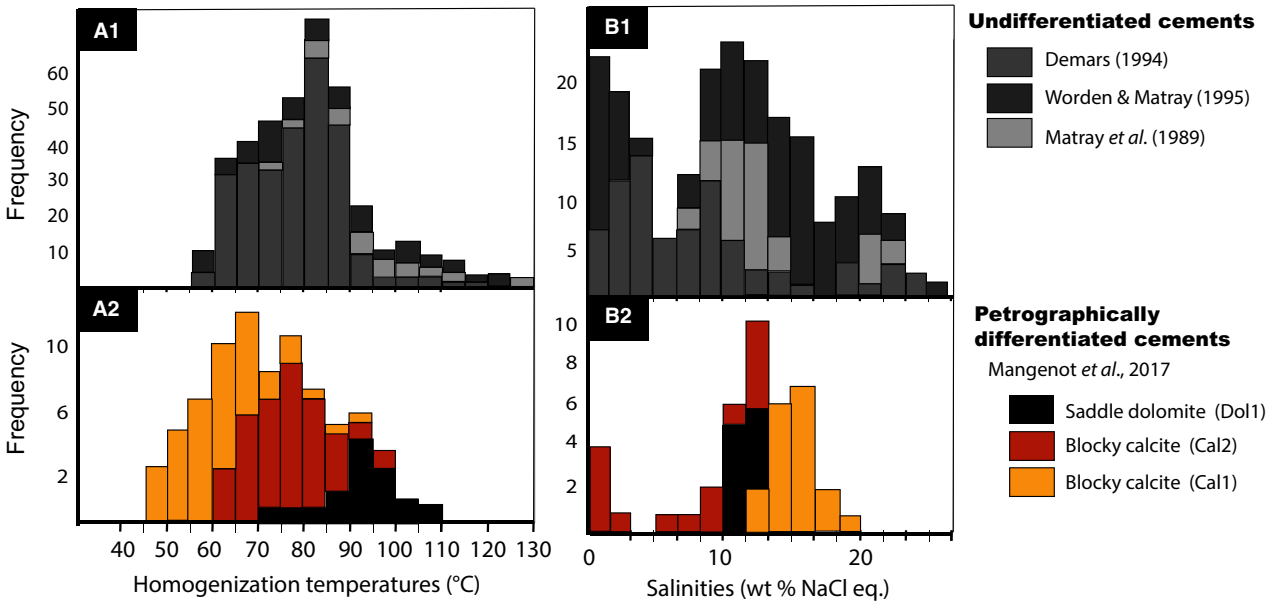

Fig. 9. Compilation of fluid inclusion microthermometry results for carbonate cements from Middle Jurassic carbonates of the Paris Basin depocentre. (A1) and (B1) Histograms of homogenization temperatures (°C) and salinities (wt% NaCl eq) acquired without petrographic phase differentiation prior to analysis (Matray *et al.*, 1989; Demars, 1994; Worden & Matray, 1995). (A2) and (B2) Histograms of homogenization temperatures and salinities acquired for the investigated cores after careful petrography and phase differentiation prior to analysis (Mangenot *et al.*, 2017). Analysed phases are from BEBJ12 and BEBJ8 samples (Cal1, Baulne en Brie), FOS1610 sample (Dol1, Fossoy) and BEBJ2 and BEBJ samples (Cal2, Baulne en Brie).

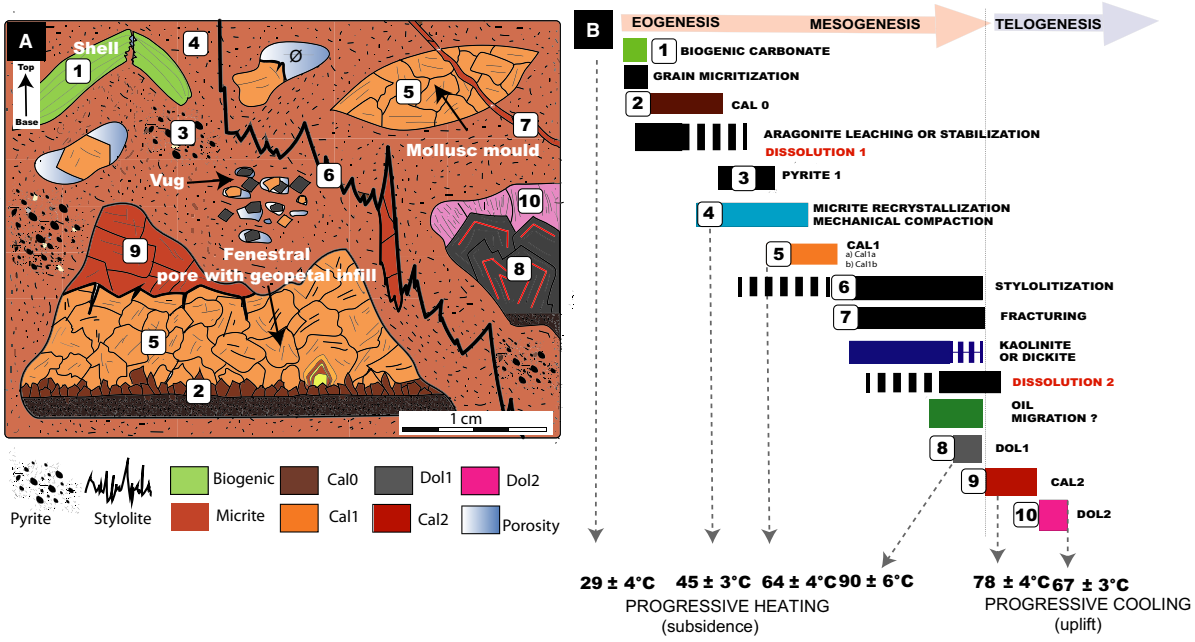

Fig. 10. (A) Schematic drawing illustrating the diagenetic evolution of the studied Middle Jurassic carbonates in the light of the Δ_{47} thermometry. (B) Temperature calibrated paragenetic sequence, including the relative timing of the investigated carbonate phases with respect to other diagenetic processes.

homogeneity possibly reflects rapid fluid circulation episodes accompanied by little interaction with the host rocks. This allowed reconstruction of a detailed thermal and compositional evolution of the fluids circulating in the Paris Basin through time, from depositional to current burial settings. The following sections interpret the findings of this survey in the framework of the known geological and hydrological history of the Paris Basin. This provided constraints on the timing of carbonate cementations, the parent fluid sources and the evolution of the water/rock systems during the main subsidence and uplift stages of the basin history.

Thermal conditions of carbonate crystallization

Based on CL microscopy, consistent petrographic features and a relative paragenetic sequence were deduced at basin scale for the different cement phases (i.e. Cal1, Dol1, Cal2 and Dol2), and a comprehensive cement stratigraphy was proposed (Fig. 5). The paragenesis was then updated considering the Δ_{47} temperatures measured on some samples of these cements and is shown in Fig. 10. Overall, the data suggest that the investigated Middle Jurassic carbonates (from four stratigraphically equivalent core intervals) recorded in a similar manner from several fluid flow episodes, leading to corresponding cementation, and spanning from Jurassic to present time. However, in some examples the CL pattern of carbonate cements was revealed not to be fully reliable to establish cement stratigraphy at basin scale (e.g. Frank *et al.*, 1995). Therefore, it should be stressed that such basin-scale cement stratigraphy correlations should preferentially rely also on geochemical data ($\delta^{18}O_{carb}$, $\delta^{13}C_{carb}$ and Δ_{47}), when possible.

Preservation of the initial TΔ_{47} and $\delta^{18}O_{water}$ values

As rocks experience elevated temperatures during deep burial and subsequent cooling during uplift, their Δ_{47} composition may be altered by solid-state reordering of C–O bonds within the mineral lattice (Passey & Henkes, 2012; Henkes *et al.*, 2014; Stolper & Eiler, 2015) and thus compromise the determination of the $\delta^{18}O_{water}$ of the parent fluid. For the carbonates studied here, the possibility of solid-state diffusion alteration can be ruled out given the three following arguments. Firstly, current knowledge on solid-state diffusion predicts that carbonate could start to lose its original Δ_{47} composition only if at *ca* 80 to 100°C for more than 100 Ma (Passey & Henkes, 2012; Stolper & Eiler, 2015), conditions that are well above those experienced by the studied carbonate unit (as independently

determined by Ménétrier *et al.*, 2005; Garibaldi, 2010; Gonçalvès *et al.*, 2010). Secondly, the excellent consistency between data from fluid inclusion microthermometry and Δ_{47} thermometry (Mangenot *et al.*, 2017), two independent methods based on different principles, strongly suggests that the measured Δ_{47} values of the carbonates were acquired at the time of crystallization. Thirdly, the bioclasts investigated here show $T\Delta_{47}$ of *ca* 29°C that agrees with growth conditions in a lagoonal setting. Consequently, the $\delta^{18}O_{water}$ of the carbonate parent fluids can be meaningfully estimated.

Syn-depositional and early diagenetic carbonates

As suggested by the preservation of primary prismatic structures of the bivalve shell and the lack of luminescence of the brachiopod shells (pristine fibres; Fig. 2A and B), the three marine bioclasts analysed do not display petrographic evidence of seawater post-depositional modifications. However, the possibility that a minor amount of syn-depositional marine cement occurs in the punctae of the brachiopod shell is not excluded. The growth temperatures of 29 ± 4°C calculated from Δ_{47} also agree with a primary marine origin, possibly reflecting Middle Jurassic seawater temperatures in a restricted lagoon environment. Seawater temperatures of 15 to 27°C were independently deduced for the Tethys ocean during Bathonian time from carbonates located at latitudes similar to those of the investigated samples (Picard *et al.*, 1998; Lécuyer, 2003).

The micrite matrix surrounding the bioclasts record $T\Delta_{47}$ of 45 ± 3°C, significantly above the 15 to 27°C surface seawater temperature expected for Middle Jurassic time (Picard *et al.*, 1998; Lécuyer, 2003). These high temperatures and the micrite negative $\delta^{18}O_{carb}$ values (−4·09 ± 0·61‰ – that are too depleted in ^{18}O compared with Middle Jurassic marine carbonates of Veizer *et al.*, 1999) could be inherited from micrites and carbonate mud recrystallization (for example, mineralogical stabilization) occurring under shallow burial conditions (as also suggested by Vincent *et al.*, 2007, and Carpentier *et al.*, 2015, for Upper Jurassic micrites in the eastern Paris Basin). An alternative hypothesis lies on the non-straightforward interpretation of Δ_{47} values from bulk samples of very fine-grained sediments, because they could reflect the natural mixing of micrite with differently sourced material, such as detrital carbonates, and early to late diagenetic cements (refer to Defliese & Lohmann, 2015, for mixing effects). In spite of these uncertainties, the recorded $T\Delta_{47}$ of 45°C dictates that at least some components of the micrite formed at temperatures higher than depositional conditions.

Burial diagenetic carbonates

Clumped isotope temperature data on 21 Cal1 cement specimens, collected from three different cores and in a wide variety of pore types and depositional environments, indicate a very homogeneous precipitation event, occurring at the basin scale under burial temperatures of 64 ± 4°C (Fig. 7). The homogeneity of $\delta^{13}C_{carb}$ and $\delta^{18}O_{carb}$ values, observed in Cal1 sub-samples over 2 cm across a representative Cal1 cement specimen (cf. Mangenot *et al.*, 2017), suggests uniform conditions for precipitation. Furthermore, the large volume of Cal1 cements precipitated in the different cores indicates a massive and pervasive fluid flow through the porous lithologies of the studied reservoir unit, mainly represented by the grain-supported facies of the *Comblanchian Formation*. This flow and consequent Cal1 cementation induced a significant porosity loss. This points to a good regional connectivity and an interconnected pore network, possibly controlled by the more porous intertidal facies, between the different wells, and thus throughout the central part of the Paris Basin. Compared to Cal1 cements, the four Dol1 cement samples record drastic changes in the CL pattern (Fig. 4B), more negative $\delta^{18}O_{carb}$ compositions and the highest $T\Delta_{47}$ of the whole paragenetic sequence (i.e. 90 ± 6°C). Such results conclusively indicate that this saddle dolomite cement was precipitated during further burial and by hotter fluids. The occurrence of possibly primary oil inclusions in some Dol1 samples (Fig. 3C) leads to the conclusion that hydrocarbons migrated synchronously with the dolomite parent fluid, at least at the Villeperdue and Fossoy core localities. The high $T\Delta_{47}$ and the oil inclusions lead to the conclusion that precipitation of Dol1 occurred close to maximum burial conditions (as deduced from Espitalie *et al.*, 1988; Guilhaumou & Gaulier, 1991; Gaulier & Burrus, 1994; Clauer *et al.*, 1995; Worden & Matray, 1995; Spötl, 1996; Gonçalvès *et al.*, 2010), also broadly corresponding to the main hydrocarbon migration phase from the source rocks (as deduced from Tremolières, 1981; Poulet & Espitalie, 1987; Espitalie *et al.*, 1988).

The two last cements of the paragenetic sequence, Cal2 and Dol2, exhibit both negative

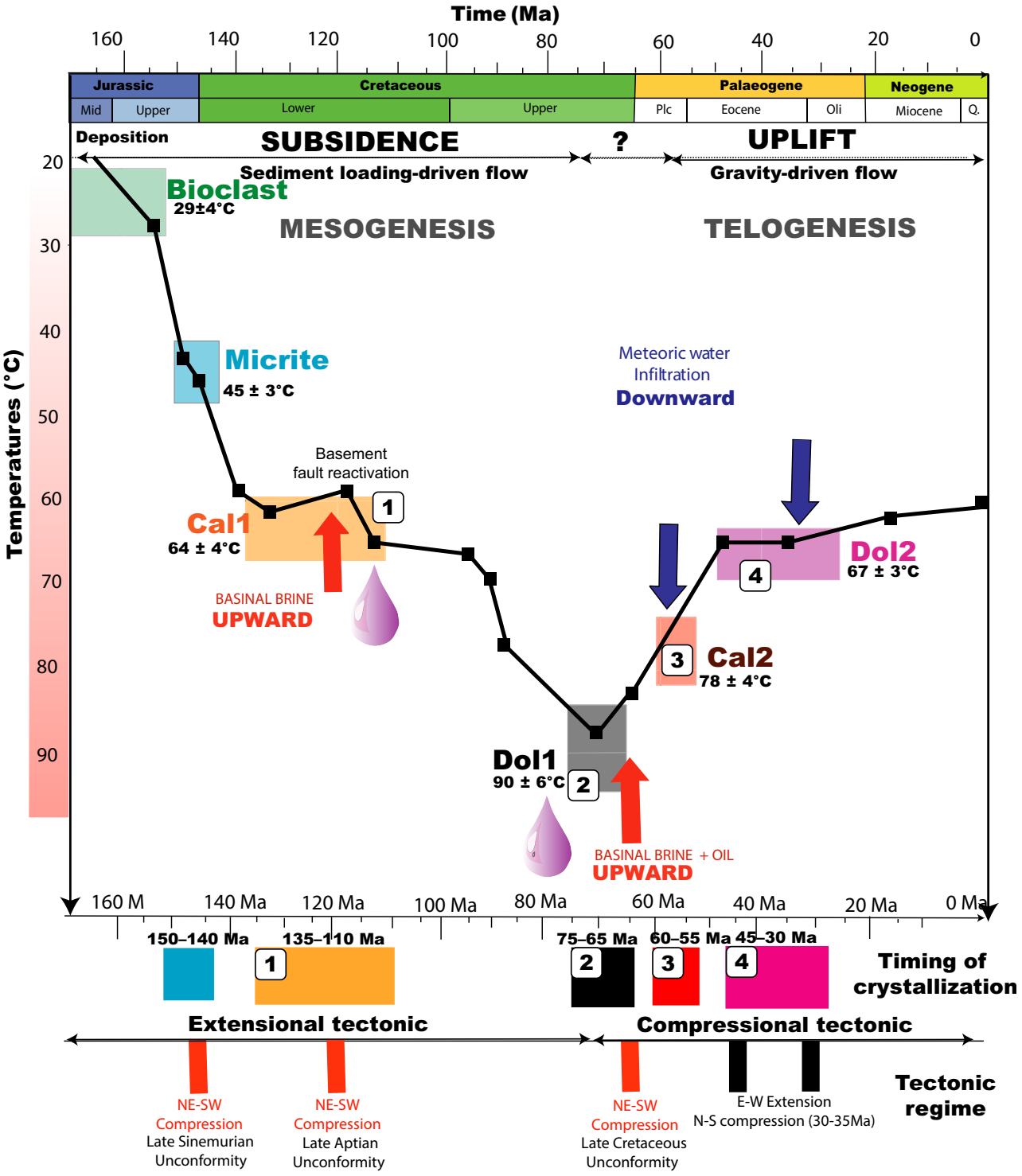

Fig. 11. Thermal and fluid flow histories for the Middle Jurassic carbonates from the Paris Basin depocentre. The black line traces the modelled thermal history (Ambreville well; Uriarte, 1997). The $T\Delta_{47}$ for Cal1, Dol1, Cal2 and Dol2, fitting the modelled thermal history, indicates possible ages for the cementation events. Basinal brine, meteoric water and oil are illustrated by pink, blue and black drops, respectively. The mechanisms supposed to drive the fluid flows are illustrated by blue (downward flow) and red (upward flow) arrows. The deduced timing of cementation is compared with the timing of main tectonic events (from Guillocheau *et al.*, 2000; André *et al.*, 2010).

$\delta^{18}O_{carb}$ values and cooler $T\Delta_{47}$ of 78 ± 4°C and 67 ± 3°C, respectively. This cooling trend is interpreted to be related to the Tertiary uplift, which is documented extensively in the Paris Basin (Guillocheau *et al.*, 2000; André *et al.*, 2010; Barbarand *et al.*, 2013). Because these two carbonate phases are volumetrically minor, the corresponding cementation events did not play an important role in the porosity reduction of the studied Middle Jurassic reservoir units.

Timing and duration of carbonate cementation

In the studied area of the Paris Basin depocentre, the thermal history of the Middle Jurassic reservoirs was already modelled (Uriarte, 1997) using BasinMod® 1D software and a palaeo-heat flow of 62 MW·m^2 at the Ambreville well locality (Figs 1E, 1F and 11). This model was constructed to force the best compromise between stratigraphic data and palaeotemperatures issued from different palaeothermometers, such as vitrinite reflectance, fluid inclusion microthermometry, Rock-Eval pyrolysis and clay mineralogy. The key features of the modelled thermal history are the increase in heating from deposition until the beginning of the Tertiary, during the subsidence-dominated stage of the basin, followed by a continuous cooling during the main uplift stage and consequent erosion (Uriarte, 1997). Because the Ambreville well is geographically close to the cores studied here (*ca* 50 to 80 km; Fig. 1E and F), located at the present-day burial depth of 1500 to 1900 m and falling within the 435 to 445°C T_{max} maturity zone (Fig. 1E and F; Delmas *et al.*, 2002), it may be considered that this well experienced burial and thermal histories similar to the four cores investigated in this study.

The thermal history reconstructed by Uriarte (1997) for the basin depocentral area can thus be used to convert the calculated $T\Delta_{47}$ into relative dates for the different carbonate cementation events, assuming a thermal equilibrium between the cement parent fluid and the host rock. The average $T\Delta_{47}$ defined for each cement phase yields uncertainties for the average ages of about ±10 Ma. Whilst the exact cementation ages may be biased, they have been derived using the same methodology and are therefore comparable. Cementation ages of 135 to 110 Ma (Lower Cretaceous) for Cal1, 75 to 65 Ma (Upper Cretaceous) for Dol1, 60 to 55 Ma (Palaeocene–Eocene) for Cal2 and 45 to 30 Ma (Eocene–Oligocene) for Dol2 (Fig. 11) were thus assumed. The ages obtained in this way confirm the paragenetic succession proposed for the different cementation events, as determined by petrographic analysis only (Figs 5 and 10). The time–temperature information derived for each carbonate cement (Fig. 11) also confirms that two of these cements (Cal1 and Dol1) precipitated during the main

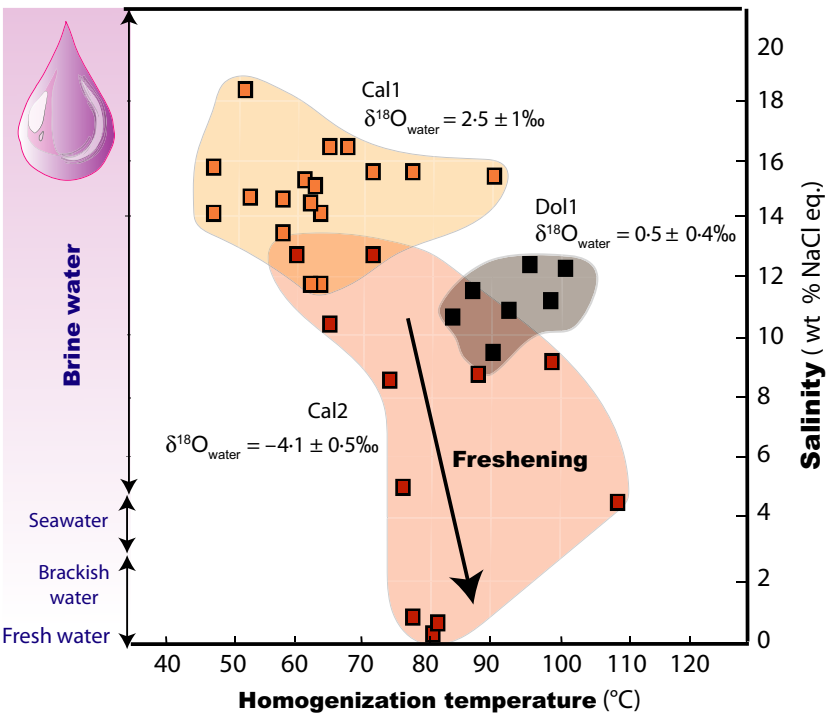

Fig. 12. Homogenization temperature versus salinity cross-plot for fluid inclusions from Cal1, Dol1 and Cal2 cements (data from Mangenot *et al.*, 2017). The average $\delta^{18}O_{water}$ values calculated for these cement phases are also reported.

Cretaceous subsidence stage, whereas the other two (Cal2 and Dol2) precipitated during the main Tertiary uplift stage.

Carbonate cementation has been interpreted both as a prolonged process that occurs slowly over a long span of time and as a rapid process, in which short bursts of activity are followed by long periods of quiescence (Tucker & Wright, 1990; Moore, 2001). Here, the inferred cementation ages (Fig. 11) indicate that cementation occurred as a rapid (<10 Ma) and episodic process, in response to punctual bursts of fluid flow activity. With the present knowledge, it is however impossible to characterize precise cementation rates.

Parent fluid geochemistry and evolution

Coupling the independent temperature estimates out of Δ_{47} data and the carbonate oxygen isotope values ($\delta^{18}O_{carb}$) allows a direct calculation of the oxygen isotope composition of the fluid ($\delta^{18}O_{water}$) from which the carbonate formed. This provides straightforward constraints on water–rock interactions that are not achievable using $\delta^{18}O_{carb}$ values only. Furthermore, when $T\Delta_{47}$ is interpreted together with fluid inclusion salinity, they can provide even better constraints on the isotope and compositional evolution of subsurface water–rock systems [see Mangenot *et al.* (2017) for a practical description of the approach], and therefore yield insights into regional groundwater fluid flows. The fluid inclusions data set produced from five samples of Cal1, Dol1 and Cal2 (Mangenot *et al.*, 2017; see synthesis in Fig. 12) are also integrated and discussed here.

Marine and early diagenetic pore-water geochemistry

In the studied Middle Jurassic carbonates, the earliest phases investigated are syn-depositional

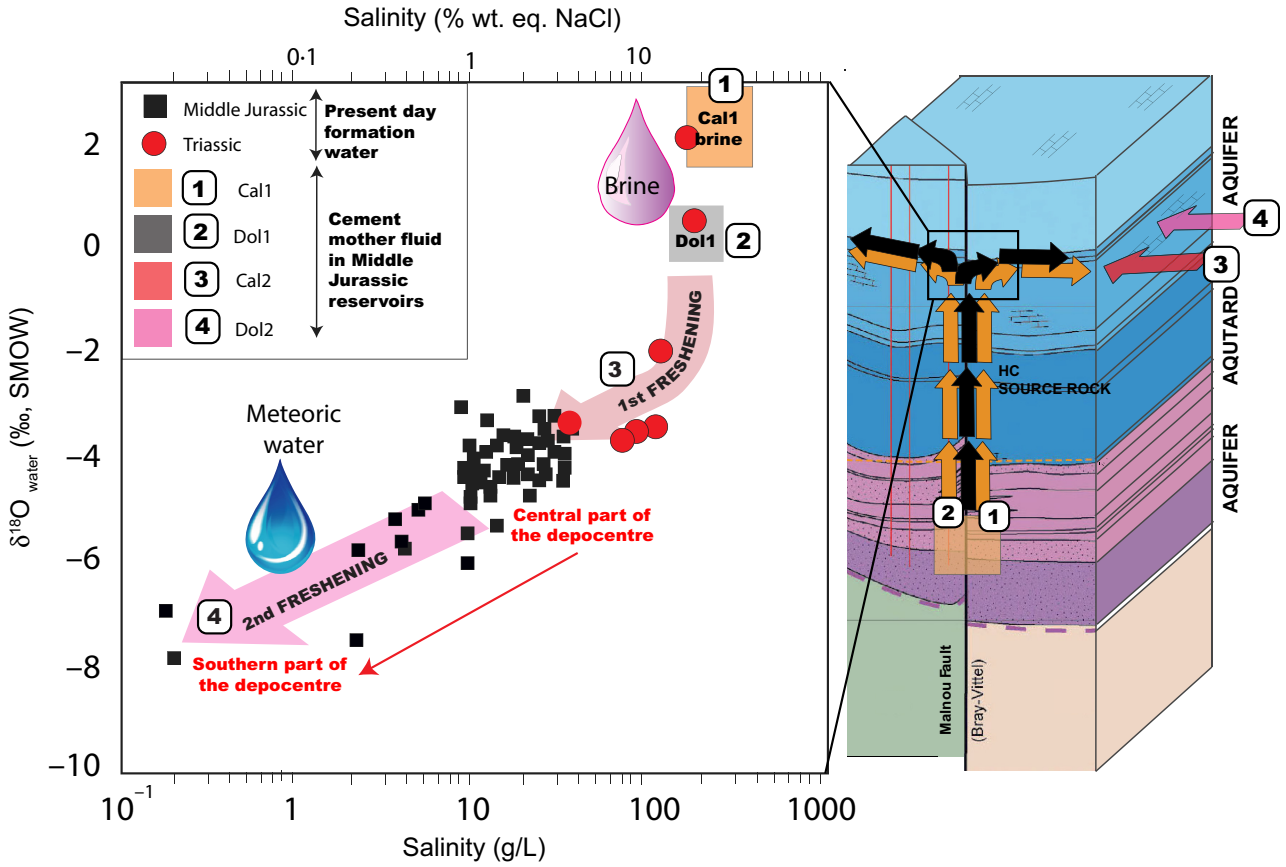

Fig. 13. Conceptual diagram showing the relative fluid flow chronology, deduced from carbonate cement geochemistry. On the left is illustrated the salinity versus $\delta^{18}O_{water}$ cross-plot, summarizing the data derived from the studied cements and those from the present-day formation waters measured by Worden & Matray (1995) and Worden *et al.* (1999). On the right is a geological block diagram with the relative timing and sources of the different fluid flows identified.

marine in origin; these are biogenic carbonates (from brachiopod and bivalve shells) and the surrounding micrites. Both carbonate groups display similar $\delta^{18}O_{water}$ values (both averaging 1·8‰; Table 1 and Fig. 8) that are in agreement with the expected isotopic composition of Jurassic seawater in restricted lagoon settings (Picard *et al.*, 1998; Lécuyer, 2003). When interpreted together with the $T\Delta_{47}$ data (Fig. 7), the $\delta^{18}O_{water}$ values indicate that the marine bioclast carbonates possibly derived from Middle Jurassic lagoon seawater at 29 ± 4°C, whereas the micrites seem to have been recrystallized at about 45 ± 3°C during burial (Fig. 11) from primary marine fluids trapped within the initial micrite pores (for example, connate waters).

Basinal brines associated with mesogenetic cements

The Cal1 mineralizing fluids are enriched in both ^{18}O and salt (with average $\delta^{18}O_{water}$ of 2·5‰ and salinity mode of 14 wt% NaCl eq; Figs 8 and 12) compared to modern seawater ($\delta^{18}O_{water}$ between −1‰ and +1‰ and salinities of 0·5 to 5 wt% NaCl eq; Rohling, 2013). Such features conjointly argue for a basinal brine origin. The Dol1 cement recorded $\delta^{18}O_{water}$ (Fig. 8) close to marine values ($\delta^{18}O_{water}$ of 0·5‰), whilst fluid inclusion salinities are about three times higher than seawater (from 10·1 to 11·5 wt% NaCl eq; Fig. 12). Such parent fluid compositions could be explained by three different scenarios: (i) a primary brine (evaporated seawater); (ii) a normal seawater which got enriched in salt and ^{18}O by water–evaporite interaction during burial; and (iii) emplacement of an externally sourced brine circulating through the sedimentary succession during burial. The first two hypotheses can be rejected based on the accepted sedimentological models for the studied Middle Jurassic reservoirs, which support the lack of both evaporitic seawater conditions and massive evaporite bodies (Purser, 1989; Javaux, 1992; Gaumet *et al.*, 1996). The data thus support the third scenario, implying the flow of externally sourced fluids through the Middle Jurassic reservoirs.

External sources of salty water in the central part of the Paris Basin could be the Upper Triassic aquifers (i.e. Chaunoy and Rhaetian sandstone reservoirs) that display present-day salinity up to 20 wt% NaCl eq and $\delta^{18}O_{water}$ up to 1·1‰ (Worden & Matray, 1995; Worden *et al.*, 1999; Millot *et al.*, 2011). Furthermore, the occurrence of a cross-formational flow between Triassic and Middle Jurassic aquifers has already been proposed in diagenetic models from previous authors (Matray *et al.*, 1994; Worden & Matray, 1995; Bril & Velde, 2000). Most importantly, this hypothesis is also supported by the geochemistry data set for Cal1 and Dol1 revealing parent fluid salinity and $\delta^{18}O_{water}$ compositions similar to the present-day groundwater of the Upper Triassic aquifers (Fig. 13; Worden & Matray, 1995; Worden *et al.*, 1999). Further geochemical investigations (^{3}He, $\delta^{34}S$, ^{14}C and trace element geochemistry) conclusively showed the occurrence of a Triassic saline component within the present-day Middle Jurassic aquifers (Marty *et al.*, 1988, 1993; Fouillac *et al.*, 1990; Wei *et al.*, 1990; Pinti & Marty, 1995; Pinti *et al.*, 1997). All of the studied subsurface cores exhibit voluminous Cal1 and Dol1 cements, with similar petrographic and geochemical features. This implies that this upward fluid migration, leading to the invasion of the Middle Jurassic reservoirs by hypersaline brines, was a widespread process that occurred at basin scale. Fluids with similar or even higher salinities than those recorded in Cal1 and Dol1 (up to 25 wt% NaCl eq; Fig. 9B.1) were indeed recorded from other cores of the basin depocentre (Matray *et al.*, 1989; Demars, 1994; Worden & Matray, 1995), allowing the extrapolation of the data set presented here at larger scale.

Some Dol1 crystals contain hydrocarbon-bearing fluid inclusions (Fig. 4C), suggesting that oil was trapped at the time of Dol1 precipitation. Such hydrocarbon-bearing fluid inclusions were not reported in previous diagenetic studies of the Paris Basin and attest that Dol1 parent fluids and oil have migrated together through the Middle Jurassic reservoirs. Because the most probable source rocks for these hydrocarbons are the underlying Lower Jurassic shales (Poulet & Espitalie, 1987; Espitalie *et al.*, 1988), the dolomitizing brine probably passed through these source rocks during the upward cross-formational flow described above. This hypothesis also satisfies the supposed mineralization age of Dol1 at 75 to 65 Ma (Fig. 11), which corresponds to the timing of peak oil generation for these source rocks (90 to 70 Ma; Monticone *et al.*, 2011).

Meteoric freshening associated with telogenetic cements

The negative $\delta^{18}O_{water}$ values determined for Cal2 and Dol2 parent fluids (averaging −4·1‰ for Cal2 and −7‰ for Dol2; Fig. 8), the salinity dilution pattern observed in Cal2 fluid inclusions (Fig. 12), as well as the different estimated

ages (Fig. 11), suggest that two distinct pulses of diluted meteoric waters occurred through the Middle Jurassic reservoirs during the Tertiary uplift of the basin. These diluted fluid pulses led to the progressive freshening of the pre-existing brines described above (refer to *Basinal brines associated with mesogenetic cements* section above). Fluids with similar low salinity (Fig. 9B.1) were indeed recorded in other cores of the basin depocentre (Demars, 1994; Worden & Matray, 1995), indicating that the influx of meteoric recharge fluids was not a local process.

These meteoric freshening pulses recorded by the last two cements of the paragenesis (i.e. the telogenetic Cal2 and Dol1) would explain why the present-day formation water in the Middle Jurassic reservoirs displays a very low saline load (around 3% total dissolved solids) and a negative $\delta^{18}O_{water}$ value (Fig. 13). Lateral recharges of meteoric waters were previously documented from the study of diagenetic cements in regions closer to the eastern margin of the basin (Buschaert *et al.*, 2004; Vincent *et al.*, 2007; Brigaud *et al.*, 2009; André *et al.*, 2010; Carpentier *et al.*, 2014). In the central part of the basin, meteoric water infiltrations were already suggested by hydrogeological modelling studies (Wei *et al.*, 1990; Gonçalvès *et al.*, 2003; Violette *et al.*, 2016), chlorine concentrations, hydrogen and oxygen isotope compositions (Matray *et al.*, 1994), and noble gas geochemistry (Castro *et al.*, 1998). However, such multiple meteoric water recharges were so far not being assessed from carbonate diagenetic cements of the central part of the basin. This meteoric water, initially cold at the recharge area (i.e. surface temperature), must have re-equilibrated with the ambient rock temperatures during circulation at depth to explain the palaeotemperatures of 78 ± 4°C and 67 ± 3°C recorded in Cal2 and Dol2 cements, respectively. In such burial conditions, the preservation of negative $\delta^{18}O_{water}$ values between −4·1‰ and −7·0‰ (typical of meteoric fluids in the Paris Basin; Matray *et al.*, 1994) could reflect high water–rock ratios, pointing to an open system behaviour (as also suggested by Lavastre *et al.*, 2011, in the eastern part of the Paris Basin). In such a context, the factors governing the switch from calcite to dolomite in the cementation sequence (Cal1–Dol1–Cal2–Dol2) cannot be easily explained.

Geodynamic control on fluid flows

In the central part of the Paris Basin, the four cementation dates estimated above (135 to 110 Ma for Cal1, 75 to 65 Ma for Dol1, 60 to 55 Ma for Cal2 and 45 to 30 Ma for Dol2; Fig. 11) correspond to well-documented periods of active tectonic stresses (i.e. Late Aptian unconformity, Late Cretaceous unconformity, Palaeocene north–south compression and Oligocene extension; Fig. 11). Such observations suggest that periods of active tectonics in the basin favoured fluid flows, leading to the precipitation of carbonate cements in the remaining pore space of the Middle Jurassic reservoirs. This geodynamic control on cementation was previously demonstrated in the Upper Jurassic carbonates of the eastern Paris Basin, located at *ca* 500 km from the studied area, which were mainly affected by meteoric cementation (Buschaert *et al.*, 2004; Gonçalvès *et al.*, 2004; Vincent *et al.*, 2007; Brigaud *et al.*, 2009; André *et al.*, 2010; Carpentier *et al.*, 2014; Blaise *et al.*, 2015).

Previous hydrogeological models agreed with the occurrence of a brine migration from the Upper Triassic to the Middle Jurassic aquifers of the studied depocentre area, though the relative timing of these upward fluid flows is still debated. Early studies (Matray *et al.*,1989) suggested an Early to Late Cretaceous timing for this cross-formational fluid flow, whereas more recent ones (Worden & Matray, 1995; Bril & Velde, 2000; Gonçalvès *et al.*, 2003; Violette *et al.*, 2016) suggested that it was a Cenozoic phenomenon, occurring during the compressional tectonic phase of the Alpine Orogeny. The novel contribution of this work, by giving access to the temperature, $\delta^{18}O_{water}$, salinity and relative timing of Cal1 and Dol1 brine migrations (Figs 7, 8 and 11 to 13), largely supports the first hypothesis (Matray *et al.*, 1989). Indeed, the findings of this study reveal that the saline load of the Middle Jurassic aquifers was due to the externally sourced parent fluids of Cal1 and Dol1, which precipitated, respectively, during Early Cretaceous (135 to 110 Ma) and Late Cretaceous (75 to 65 Ma) time, in a dominantly subsiding context. During subsidence stages of basin evolution, pore fluid pressure tends to increase and may favour upward fluid flows. Permeable fault zones may then act as drains for fluids to move. In this respect, Cal1 and Dol1 parent fluids could have been channelled from the Upper Triassic donor aquifers towards the Middle Jurassic receiver aquifers by such upward flow along faults (Fig. 13B). Interestingly, Guillocheau *et al.* (2000) have demonstrated that the Variscan Bray fault system (Fig. 1C), cross-cutting the basin depocentre,

experienced different episodes of reactivation during Lower and Upper Cretaceous times, largely supporting the reliability of the proposed fluid flow scenario. The Cretaceous timing of brine migration, inferred for Cal1 and Dol1 parent fluids in the central part of the basin, can also be temporally related to carbonate cementation events previously identified in the eastern and southern margins of the Paris Basin (Brigaud *et al.*, 2009; Gigoux *et al.*, 2015), as well as in the Wessex Basin of southern England (Hendry, 1993; Worden *et al.*, 2016), the latter being the extension of the Paris Basin to the north. Indeed, Gigoux *et al.* (2015) reported a major fluid flow leading to fluorine mineralization in the southern Paris Basin at 130 ± 15 Ma (from Sm–Nd dating), whereas Brigaud *et al.* (2009) reported a contemporaneous meteoric water input, leading to carbonate cements, at the Aptian–Albian transition in Upper Jurassic strata of the eastern margin of the basin. Cretaceous fluid flows with meteoric affinity have also been documented in the Middle Jurassic strata of the Wessex Basin in southern England (Hendry, 1993; Worden *et al.*, 2016). When all of these studies are integrated together, they provide strong evidence of multiple and tectonically controlled fluid flows during Cretaceous time that led to massive movements of differently sourced waters through the different carbonate units of the Paris Basin.

Successively, tectonic inversion occurred in the Paris Basin, mainly linked to the beginning of the Pyrenean compression at the Late Cretaceous to Palaeogene boundary (Barbarand *et al.*, 2013). These geodynamic changes induced the exposure of the basin margins and a drastic modification in the fluid flow mechanisms that would have favoured lateral infiltrations of surface-derived waters at depth (i.e. meteoric recharge; see for instance Garven & Freeze, 1984). The findings here agree with this hypothesis and demonstrate that Cal2 and Dol2 (the last two cement phases of the paragenesis) have been precipitated by meteoric-derived fluids during Palaeocene–Eocene (60 to 55 Ma) and Eocene–Oligocene (45 to 30 Ma) times, respectively. The mixing of these meteoric waters with the pre-existing hypersaline groundwater implies a topography-driven fluid flow, with a sufficiently high hydraulic gradient, and a well-interconnected pore network to channel the fluids from surface to depth (more than 1500 m) along several hundreds of kilometres. Dorobek (1987) described Silurian meteoric cements in basinal limestones of the central Appalachians precipitated at least 150 km away from the inferred recharge area, in tectonically uplifted basin margins, buried beneath some 250 m of low permeable strata. The broadly similar scale of this process suggests that, in the Paris Basin, Tertiary telogenetic meteoric waters would have been capable of rapidly extending through the Middle Jurassic strata at basin scale, to reach the deepest parts of the basin centre. However, the results of isotope analysis on present-day formation waters (Fig. 13) show that the Middle Jurassic aquifers were not completely flushed away by the infiltrated Tertiary meteoric waters (Matray *et al.*, 1994). This suggests that the hydraulic head, triggering the meteoric recharge fluid flow, was not sufficiently high to cause the complete flushing of the pre-existing brines, possibly due to the lack of a high-relief highland.

To conclude, when the whole Paris Basin hydrogeological scenario is considered, it shares numerous similarities with the fluid flow histories recorded in other intracratonic basins with comparable architecture, such as the Illinois Basin (Stueber & Walter, 1994; Labotka *et al.*, 2015) or the Michigan Basin (Wilson & Long, 1993). Indeed, these basins also experienced late stage infiltration of meteoric fluids into more ancient saline evaporative waters. Therefore, the combination of clumped isotope thermometry with conventional petrography and fluid inclusion studies on carbonate burial cements could serve as a powerful investigation approach to achieve a more detailed reconstruction of the hydrogeological histories and water–rock interactions in other sedimentary basins.

CONCLUSIONS

Middle Jurassic carbonates from the central part of the Paris Basin were investigated based on a sample collection from four subsurface cores (present depth of 1500 to 1900 m). The thermal and diagenetic evolution of this stratigraphic interval was precisely reconstructed using petrographic observations combined with extensive Δ_{47} analyses for each identified carbonate phase.

The implications of the collected data can be summarized as follows:

1 Sedimentation occurred from slightly evaporated seawater in a lagoonal setting ($\delta^{18}O_{water}$ of 1·8 ± 1·4‰) at temperatures of 29 ± 4°C.

2 Syn-sedimentary micrites record recrystallization during burial at higher temperatures

(close to 45°C) from connate waters also enriched in ^{18}O ($\delta^{18}O_{water}$ of 2·3 ± 0·7‰).

3 A first major pore-filling calcite cementation phase (Cal1) precipitated at 64 ± 4°C, from high salinity fluids (14 wt% NaCl eq) with a $\delta^{18}O_{water}$ close to 2·5‰, pointing to a primary brine.

4 A second cementation phase induced dolomite (Dol1) precipitation at 90 ± 6°C, from similar fluids with moderate salinity (11 wt% NaCl eq) and a $\delta^{18}O_{water}$ value of 0·5 ± 0·4‰, coeval with hydrocarbon reservoir charging.

5 A third cementation phase resulted in calcite precipitation (Cal2) at 78 ± 4°C associated with the circulation of meteoric-derived fluids, with low salinity (from 12 to 0 wt% NaCl eq) and a $\delta^{18}O_{water}$ value of −4·1 ± 0·5‰.

6 A fourth and last cementation phase led to the formation of dolomite (Dol2) at temperatures of 67 ± 3°C by meteoric-derived fluids with a negative $\delta^{18}O_{water}$ value of −7·0 ± 0·8‰.

The thermal information and fluid properties obtained by Δ_{47} thermometry are consistent with the burial, hydrogeological and tectonic evolution known for the Paris Basin and allow refinement of previous diagenetic models. Findings in this study imply two major brine circulation episodes in Early (Cal1) and Late (Dol1) Cretaceous times, during the main subsidence phase, followed by two diluted water influxes (Cal2 and Dol2), during the Tertiary basin inversion and consequent uplift. The $\delta^{18}O_{water}$ and salinity for Cal1 and Dol1 parent fluids indicate a likely contribution of Triassic reservoir fluids that reached the Middle Jurassic lithologies through a cross-formational flow along major faults, such as the Bray fault system. Conversely, $\delta^{18}O_{water}$ and salinity for Cal2 and Dol2 parent fluids indicate a freshening of the Middle Jurassic reservoirs by a topography-driven flow during the Tertiary, from an unknown meteoric recharge area.

Overall, the results demonstrate how a careful petrographic characterization is an important prerequisite for identifying individual carbonate cementation phases at basin scale, and to apply the carbonate clumped isotope (Δ_{47}) thermometry at its highest level of performance (in terms of both accuracy and precision on temperature and $\delta^{18}O_{water}$ of the carbonate parent fluids). Such study permits the refinement of constraints on the fluid flow and water–rock system evolution at the basin scale. More broadly, this study also illustrates how Δ_{47} thermometry provides information of primary importance to constrain carbonate diagenesis that largely extends what is currently achievable with conventional isotopic and petrographic data alone. The use of Δ_{47} thermometry on diagenetic cements is a powerful tool to investigate fluid flows and palaeothermicity, thereby addressing a longstanding conundrum in basin research.

ACKNOWLEDGEMENTS

We thank Carine Chaduteau and Amandine Katz for help with Δ_{47} measurements at IPGP. We are also grateful to Magali Ader, Pascal Houel, Geneviève Bessereau, Benjamin Brigaud, Jean-Pierre Girard and Christophe Durlet for the constructive discussions about the thermicity, the diagenesis and fluid flow histories of the Paris Basin. The subsurface cores of Baulne en Brie, Rigny la Nonneuse and Fossoy were available from the IFPEN storage collection of the BEPH (*Bureau Exploration-Production d'Hydrocarbures*). The Villeperdue subsurface core was available from the University of Dijon. We are also grateful to Alain Buisson and Pierre André Duboin from Lundin Petroleum for sharing their knowledge on the petroleum reservoirs of the Paris Basin.

REFERENCES

Affolter, S., **Fleitmann, D.** and **Leuenberger, M.** (2014) New online method for water isotope analysis of speleothem fluid inclusions using laser absorption spectroscopy (WS-CRDS). *Clim. Past*, **10**, 1291–1304.

André, G., **Hibsch, C.**, **Fourcade, S.**, **Cathelineau, M.** and **Buschaert, S.** (2010) Chronology of fracture sealing under a meteoric fluid environment: microtectonic and isotopic evidence of major Ceinozoic events in the eastern Paris Basin (France). *Tectonophysics*, **490**, 214–228.

Barbarand, J., **Quesnel, F.** and **Pagel, M.** (2013) Lower Paleogene denudation of Upper Cretaceous cover of the Morvan Massif and southeastern Paris Basin (France) revealed by AFT thermochronology and constrained by stratigraphy and paleosurfaces. *Tectonophysics*, **608**, 1310–1327.

Blaise, T., **Tarantola, A.**, **Cathelineau, M.**, **Boulvais, P.**, **Techer, I.**, **Rigaudier, T.**, **Boiron, M.C.**, **Pierron, O.** and **Landrein, P.** (2015) Evolution of porewater composition through time in limestone aquifers: salinity and D/H of fluid inclusion water in authigenic minerals (Jurassic of the eastern Paris Basin, France). *Chem. Geol.*, **417**, 210–227.

Bonifacie, M., **Calmels, D.**, **Eiler, J.M.**, **Horita, J.**, **Chaduteau, C.**, **Vasconcelos, C.**, **Agrinier, P.**, **Katz, A.**, **Passey, B.H.**, **Ferry, J.M.** and **Bourand, J.J.** (2017) Experimental calibration of the dolomite clumped isotope thermometer from 25 to 350°C, and implications for the temperature estimates for all (Ca, Mg, Fe) CO_3 carbonates digested at high temperature. *Geochim. Cosmochim. Acta*, **200**, 255–279.

Brand, W.A., **Assonov, S.S.** and **Coplen, T.B.** (2010) Correction for the ^{17}O interference in $\delta(^{13}C)$ measurements when analyzing CO_2 with stable isotope mass spectrometry. *Pure Appl. Chem.*, **82**, 1719–1733.

Brigaud, B., **Durlet, C.**, **Deconinck, J.-F.**, **Vincent, B.**, **Thierry, J.** and **Trouiller, A.** (2009) The origin and timing of multiphase cementation in carbonates: impact of regional scale geodynamic events on the Middle Jurassic Limestones diagenesis (Paris Basin, France). *Sediment. Geol.*, **222**, 161–180.

Bril, H. and **Velde, B.** (2000) Effects of the 'Pays De Bray' fault on fluid paleocirculations in the Paris Basin Dogger Reservoir, France. *Science*, **23**, 305–315.

Bristow, T.F., **Bonifacie, M.**, **Derkowski, A.**, **Eiler, J.M.** and **Grotzinger, J.P.** (2011) A hydrothermal origin for isotopically anomalous cap dolostone cements from south China. *Nature*, **474**, 68–71.

Brunet, M.F. and **Le Pichon, X.** (1982) Subsidence of the Paris Basin. *J. Geophys. Res.*, **87**, 8547–8560.

Budd, D.A., **Frost, E.L.**, **Huntington, K.W.** and **Allwardt, P.F.** (2013) Syndepositional deformation features in high-relief carbonate platforms: long-lived conduits for diagenetic fluids. *J. Sediment. Res.*, **83**, 12–36.

Buschaert, S., **Fourcade, S.**, **Cathelineau, M.**, **Deloule, E.**, **Martineau, F.**, **Ayt Ougougdal, M.** and **Trouiller, A.** (2004) Widespread cementation induced by inflow of continental water in the eastern part of the Paris Basin: O and C isotopic study of carbonate cements. *Appl. Geochem.*, **19**, 1201–1215.

Carpentier, C., **Brigaud, B.**, **Blaise, T.**, **Vincent, B.**, **Durlet, C.**, **Boulvais, P.** and **Pagel, M.** (2014) Impact of basin burial and exhumation on Jurassic carbonates diagenesis on both sides of a thick clay barrier (Paris Basin, NE France). *Mar. Pet. Geol.*, **53**, 44–70.

Carpentier, C., **Ferry, S.**, **Lecuyer, C.**, **Strasser, A.**, **Geraud, Y.** and **Trouiller, A.** (2015) Origin of micropores in Late Jurassic (Oxfordian) micrites of the Eastern Paris Basin, France. *J. Sediment. Res.*, **85**, 660–682.

Castro, M.C., **Goblet, P.**, **Ledoux, E.**, **Violette, S.** and **De Marsily, G.** (1998) Noble gases as natural tracers of water circulation in the Paris Basin: 2. Calibration of a groundwater flow model using noble gas isotope data. *Water Resour. Res.*, **34**, 2467–2483.

Chantraine, J., **Autran, A.**, **Cavelier, C.**, **Alabouvette, B.**, **Barféty, J.C.**, **Cecca, F.**, **Clozier, L.**, **Debrand-Passard, S.**, **Dubreuilh, J.**, **Feybesse, J.L.**, **Guennoc, P.**, **Ledru, P.**, **Rossi, P.** and **Ternet, Y.** (1996). Carte géologique de la France. 1/1 000 000, BRGM, Orléans.

Choquet, P.W. and **Pray, L.C.** (1970) Geologic nomenclature and classification of porosity in sedimentary carbonates. *AAPG Bull.*, **54**, 207–250.

Clauer, N., **O'Neil, J.R.** and **Furlan, S.** (1995) Clay minerals as records of temperature conditions and duration of thermal anomalies in the Paris Basin, France. *Clay Miner.*, **30**, 1–13.

Daëron, M., **Blamart, D.**, **Peral, M.** and **Affek, H.** (2016) Absolute isotopic abundance ratios and the accuracy of Δ_{47} measurements. *Chem. Geol.*, **442**, 83.

Dale, A., **John, C.M.**, **Mozley, P.S.**, **Smalley, P.C.** and **Muggeridge, A.H.** (2014) Time-capsule concretions: unlocking burial diagenetic processes in the Mancos Shale using carbonate clumped isotopes. *Earth Planet. Sci. Lett.*, **394**, 30–37.

Defliese, W.F. and **Lohmann, K.C.** (2015) Non-linear mixing effects on mass-47 CO_2 clumped isotope thermometry: patterns and implications. *Rapid Commun. Mass Spectrom.*, **29**, 901–909.

Delmas, J., **Houel, P.** and **Vially, R.** (2002) Paris Basin. Rapport régional d'évaluation pétrolière. *IFPEN intern report.* 172 pp.

Demars, C. (1994) Évolution diagénétique, paléofluides et paléothermicité dans les réservoirs du Keuper et du Dogger du bassin de Paris. *Thesis, INPL, 325* pp.

Dennis, K.J., **Affek, H.P.**, **Passey, B.H.**, **Schrag, D.P.** and **Eiler, J.M.** (2011) Defining an absolute reference frame for 'clumped' isotope studies of CO2. *Geochim. Cosmochim. Acta*, **75**, 7117–7131.

Dorobek, S.L. (1987) Petrography, geochemistry, and origin of burial diagenetic facies, Siluro-Devonian Helderberg Group (carbonate rocks), Central Appalachians. *Am. Assoc. Petrol. Geol.*, **71**, 492–514.

Eiler, J.M. (2007) 'Clumped-isotope' geochemistry-The study of naturally-occurring, multiply-substituted isotopologues. *Earth Planet. Sci. Lett.*, **262**, 309–327.

Epstein, S., **Buchsbaum, R.**, **Lowenstam, H.** and **Urey, H.** (1951) Carbonate-water isotopic temperature. *Bull. Geol. Soc. Am.*, **62**, 417–426.

Espitalie, J., **Maxwell, J.R.**, **Chenet, Y.** and **Marquis, F.** (1988) Aspects of hydrocarbon migration in the Mesozoic in the Paris Basin as deduced from an organic geochemical survey. *Org. Geochem.*, **13**, 467–482.

Flugel, E. (2004) *Microfacies of Carbonate Rocks. Analysis, Interpretation and Application.* Springer-Verlag, Berlin, Heidelberg, 976 pp.

Fontes, J.C. and **Matray, J.M.** (1993) Geochemistry and origin of formation brines from the Paris Basin, France. *Chem. Geol.*, **109**, 149–175.

Fouillac, C., **Fouillac, A.M.** and **Criaud, A.** (1990) Sulphur and oxygen isotopes of dissolved sulphur species in formation waters from the Dogger geothermal aquifer, Paris Basin, France. *Appl. Geochem.*, **5**, 415–427.

Frank, T.D., **Lohmann, K.C.** and **Meyers, W.J.** (1995) Chronostratigraphic significance of cathodoluminescence zoning in syntaxial cement: Mississippian Lake Valley Formation, New Mexico. *Sed. Geol.*, **105**, 29–50.

Garibaldi, C. (2010) Détermination des températures profondes du bassin du Sud-Est de la France et relations entre anomalies thermiques, géologie et circulations hydrothermales par modelisation 3D.Thesis Université Nice Sophia Antipolis, 288 pp.

Garven, G. and **Freeze, R.A.** (1984) Theoretical analysis of the role of groundwater flow in the genesis of strata bound ore deposits. *Am. J. Sci.*, **284**, 1125–1174.

Gaulier, J.M. and **Burrus, J.** (1994) Modeling present and past thermal regimes in the Paris Basin - petroleum implications. *Hydrocarb. Pet. Geol. Fr.*, **25**, 61–75.

Gaumet, F. (1997) Fondements géologiques pour la modélisation stratigraphique des systèmes carbonatés. Le Jurassique moyen de l'Angleterre à la Méditerranée, *Thèse, Université C. Bernard – Lyon*, 290 pp.

Gaumet, F., **Garcia, J.P.**, **Dromart, G.** and **Sambet, G.** (1996) Contrôle stratigraphique des faciès, géométries et profils de dépôt de la plate-forme carbonatée bourguignonne au Bathonien-Callovien. *Bull. Soc. Géol. Fr.*, **167**, 409–421.

Gely, J-P. and **Hanot, F.** (2014) Le bassin parisien: un nouveau regard sur la géologie. In: *Bulletin d'information des géologues du bassin de Paris*, 9, 229 pp.

Gigoux, M., **Delpech, G.**, **Guerrot, C.**, **Pagel, M.**, **Augé, T.**, **Négrel, P.** and **Brigaud, B.** (2015) Evidence for an Early Cretaceous mineralizing event above the basement/

sediment unconformity in the intracratonic Paris Basin: paragenetic sequence and Sm-Nd dating of the world-class Pierre-Perthuis stratabound fluorite deposit. *Miner. Depos.*, **50**, 455–463.

Goldstein, R. and **Reynolds, J.** (1994) Systematics of Fluid Inclusions. *SEPM Short Course Notes, 31*, 188 pp.

Gonçalvès, J., **Violette, S.**, **Robin, C.**, **Pagel, M.**, **Guillocheau, F.**, **de Marsily, G.**, **Bruel, D.** and **Ledoux, E.** (2003) 3-D modelling of salt and heat transport during the 248 m.y. evolution of the Paris Basin; diagenetic implications. *Bull. Soc. Geol. Fr.,* **174**, 429–439.

Gonçalvès, J., **Violette, S.**, **Guillocheau, F.**, **Robin, C.**, **Pagel, M.**, **Bruel, D.**, **de Marsily, G.** and **Ledoux, E.** (2004) Contribution of a three-dimensional regional scale basin model to the study of the past fluid flow evolution and the present hydrology of the Paris basin, France. *Basin Res.*, **16**, 569–586.

Gonçalvès, J., **Pagel, M.**, **Violette, S.**, **Guillocheau, F.** and **Robin, C.** (2010) Fluid inclusions as constraints in a three-dimensional hydro-thermo-mechanical model of the Paris basin, France. *Basin Res.*, **22**, 699–716.

Guettard, J.E. (1746) Mémoire et carte minéralogique sur la nature et la situation des terrains qui traversent la France et l'Angleterre. *Mém. Acad. Roy. Sci.*, **12**, 363–393.

Guilhaumou, N. and **Gaulier, J.M.** (1991) Détermination de paléotempératures dans les roches-mères du bassin de Paris: etude d'inclusions fluides et implications pour l'histoire thermique du bassin. *Compte. R. Acad. Sci. Paris*, **42**, 773–780.

Guillocheau, F., **Robin, C.**, **Allemand, P.**, **Bourquin, S.**, **Brault, N.**, **Dromart, G.**, **Friedenberg, R.**, **Garcia, J.P.**, **Gaulier, J.M.** and **Gaumet, F.** (2000) Meso-Cenozoic geodynamic evolution of the Paris Basin: 3D stratigraphic constraints. *Geodin. Acta*, **13**, 189–245.

Hendry, J.P. (1993) Geological control on regional subsurface carbonate cementation: an isotopic paleohydrologic investigation of middle Jurassic limestones in Central England. In: *Diagenesis and Basin Development* (Eds A.D. Horbury and A.G. Robinson), **36**, pp. 231–260. AAPG Studies in Geology, USA.

Henkes, G.A., **Passey, B.H.**, **Wanamaker, A.D.**, **Grossman, E.L.**, **Ambrose, W.G.** and **Carroll, M.L.** (2013) Carbonate clumped isotope compositions of modern marine mollusk and brachiopod shells. *Geochim. Cosmochim. Acta*, **106**, 307–325.

Henkes, G.A., **Passey, B.H.**, **Grossman, E.L.**, **Shenton, B.J.**, **Pérez-Huerta, A.** and **Yancey, T.E.** (2014) Temperature limits for preservation of primary calcite clumped isotope paleotemperatures. *Geochim. Cosmochim. Acta*, **139**, 362–382.

Horita, J. (2014) Oxygen and carbon isotope fractionation in the system dolomite–water–CO2 to elevated temperatures. *Geochim. Cosmochim. Acta*, **129**, 111–124.

Huntington, K.W. and **Lechler, A.R.** (2015) Carbonate clumped isotope thermometry in continental tectonics. *Tectonophysics*, **647–648**, 1–20.

Huntington, K.W., **Budd, D.A.**, **Wernicke, B.P.** and **Eiler, J.M.** (2011) Use of clumped-isotope thermometry to constrain the crystallization temperature of diagenetic calcite. *J. Sediment. Res.*, **81**, 656–669.

Javaux, C. (1992) La plateforme parisienne et bourguignonne au Bathonien terminal et au Callovien. Thesis, *Mém. Géol. Univ. Dijon,* 365 pp.

Katz, A., **Bonifacie, M.**, **Hermoso, M.** and **Calmels, D.** (2017) Laboratory-grown coccoliths exhibit no vital effect in clumped isotope (Δ_{47}) composition on a range of geologically relevant temperatures. *Geochim. Cosmochim. Acta*, **208**, 335–353.

Kluge, T., **John, C.M.**, **Jourdan, A.-L.**, **Davis, S.** and **Crawshaw, J.** (2015) Laboratory calibration of the calcium carbonate clumped isotope thermometer in the 25–250°C temperature range. *Geochim. Cosmochim. Acta*, **157**, 213–227.

Labotka, D.M., **Panno, S.V.**, **Locke, R.A.** and **Freiburg, J.T.** (2015) Isotopic and geochemical characterization of fossil brines of the Cambrian Mt. Simon Sandstone and Ironton-Galesville Formation from the Illinois Basin, USA. *Geochim. Cosmochim. Acta*, **165**, 342–360.

Lavastre, V., **Ader, M.**, **Buschaert, S.**, **Petit, E.** and **Javoy, M.** (2011) Water circulation control on carbonate-δ18O records in a low permeability clay formation and surrounding limestones: the Upper Dogger-Oxfordian sequence from the eastern Paris Basin, France. *Appl. Geochem.*, **26**, 818–827.

Lécuyer, C. (2003) Thermal evolution of Tethyan surface waters during the Middle-Late Jurassic: evidence from δ^{18} O values of marine fish teeth. *Paleoceanography*, **18**, 1076.

Loyd, S.J., **Corsetti, F.A.**, **Eiler, J.M.** and **Tripati, A.K.** (2012) Determining the diagenetic conditions of concretion formation: assessing temperatures and pore waters using clumped isotopes. *J. Sediment. Res.*, **82**, 1006–1016.

Loyd, S.J., **Corsetti, F.A.**, **Eagle, R.A.**, **Hagadorn, J.W.**, **Shen, Y.**, **Zhang, X.**, **Bonifacie, M.** and **Tripati, A.K.** (2015) Evolution of Neoproterozoic Wonoka-Shuram anomaly-aged carbonates: evidence from clumped isotope paleothermometry. *Precambrian Res.*, **264**, 179–191.

Mangenot, X., **Bonifacie, M.**, **Gasparrini, M.**, **Goetz, A.**, **Chaduteau, C.**, **Ader, M.** and **Rouchon, V.** (2017) Coupling Δ_{47} and fluid inclusion thermometry on carbonate cements to precisely reconstruct the temperature, salinity and δ^{18}O of paleo-groundwater in sedimentary basins. *Chem. Geol.*, **472**, 44–57.

Marty, B., **Criaud, A.** and **Fouillac, C.** (1988) Low enthalpy geothermal fluids from the Paris sedimentary basin—1. Characteristics and origin of gases. *Geothermics*, **17**, 619–633.

Marty, B., **Torgersen, T.**, **Meynier, V.**, **O'Nions, R.K.** and **De Marsily, G.** (1993) Helium isotope fluxes and groundwater ages in the Dogger Aquifer, Paris Basin. *Water Resour. Res.*, **29**, 1025–1035.

Matray, J.M., **Meunier, A.**, **Thomas, M.** and **Fontes, J.C.** (1989) The Triassic and Dogger formation waters from the Paris Basin: history and diagenetic effects upon the reservoirs. *Soc. Nat. Elf-Aquitaine – Internal Report*, 13, 484-504.

Matray, J.M., **Lambert, M.** and **Fontes, J.C.** (1994) Stable isotope conservation and origin of saline waters from the Middle Jurassic aquifer of the Paris Basin, France. *Appl. Geochem.*, **9**, 297–309.

McCrea, J.M. (1950) On the isotopic chemistry of carbonates and a paleotemperature. *J. Chem. Phys.*, **18**, 849.

Ménétrier, C., **Élie, M.**, **Martinez, L.** and **Le, A.** (2005) Estimation of the maximum burial palaeotemperature for Toarcian and Callovo-Oxfordian samples in the central part of the Paris Basin using organic markers. *Comptes Rendus Geosci.*, **337**, 1323–1330.

Millot, R., **Guerrot, C.**, **Innocent, C.**, **Philippe, N.** and **Sanjuan, B.** (2011) Chemical, multi-isotopic (Li-B-Sr-U-O) and thermal characterization of Triassic formation waters from the Paris Basin. *Chem. Geol.*, **283**, 226–241.

Monticone, B., **Duval, M.**, **Knispel, R.**, **Wojciak, P.** and **Dubille, M.H.** (2011) Shale oil potential of the Paris Basin, France. *AAPG Int. Conf. Exhib,* 10384.

Moore, C. (2001) Carbonate Reservoirs: Porosity, Evolution and Diagenesis in a Sequence Stratigraphic Framework. *Developments in Sedimentology 55, Elsevier Science, Amsterdam*. 460 pp.

Morse, J.W. and **Mckenzie, F.T.** (1990) Geochemistry of Sedimentary Carbonates. *Developments in Sedimentology, 48, Elsevier Science, Amsterdam*. 760 pp.

O'Neil, J.R. (1969) Equilibrium and nonequilibrium oxygen isotope effects in synthetic carbonates. *Geochim. Cosmochim. Acta*, **61**, 3461–3475.

Passey, B.H. and **Henkes, G.A.** (2012) Carbonate clumped isotope bond reordering and geospeedometry. *Earth Planet. Sci. Lett.*, **351**, 223–236.

Passey, B.H., **Levin, N.E.**, **Cerling, T.E.**, **Brown, F.H.** and **Eiler, J.M.** (2010) High temperature environments of human evolution in East Africa based on bond reordering in paleosol carbonates. *Proc. Natl Acad. Sci.*, **107**, 11245–11249.

Perrodon, A. and **Zabek, J.** (1991) Paris Basin. In: *IntraCratonic Basins, Mem. Am. Ass. Pet. Geol. 51*, 633–679.

Picard, S., **Garcia, J.P.**, **Lécuyer, C.**, **Sheppard, S.M.F.**, **Cappetta, H.** and **Emig, C.C.** (1998) $\delta^{18}O$ values of coexisting brachiopods and fish: temperature differences and estimates of paleo-water depths. *Geology*, **26**, 975–978.

Pinti, D.L. and **Marty, B.** (1995) Noble gases in crude oils from the Paris Basin, France: implications for the origin of fluids and constraints on oil-water-gas interactions. *Geochim. Cosmochim. Acta*, **59**, 3389–3404.

Pinti, D.L., **Marty, B.** and **Andrews, J.N.** (1997) Atmosphere-derived noble gas evidence for the preservation of ancient waters in sedimentary basins. *Geology*, **25**, 111–114.

Pomerol, C. (1989) Naissance et développement de la Géologie du Bassin Parisien au cours des XVIIe et XIXe siècles. *Bull. Inf. Géol. Bass. Paris*, **26**, 9–20.

Poulet, M. and **Espitalie, J.** (1987) Hydrocarbon migration in the Paris Basin. In: *Migration of Hydrocarbons in Sedimentary Basins* (Ed. B. Doligez), **45**, pp. 131–171. Institut Francais Du Petrole Publications, Editions Technip, France.

Purser, B.H. (1989) Plateformes carbonatées: exemple du Jurassique Moyen du Bassin de Paris. Dynamique et méthodes d'étude des bassins sédimentaires. *In: Association des sédimentologistes français. Editions Technip*, pp. 145–163.

Rohling, E.J. (2013) Oxygen isotope composition of seawater. *Encycl. Quat. Sci.*, **2**, 915–922.

Rosenbaum, J. and **Sheppard, S.M.** (1986) An isotopic study of siderites, dolomites and ankerites at high temperatures. *Geochim. Cosmochim. Acta*, **50**, 1147–1150.

Santrock, J., **Studley, S.A.** and **Hayes, J.M.** (1985) Isotopic analyses based on the mass spectrum of carbon dioxide. *Anal. Chem.*, **57**, 1444–1448.

Schauer, A.J., **Julia Kelson, J.**, **Saenger, C.** and **Huntington, K.W.** (2016) Choice of ^{17}O correction affects clumped isotope (Δ_{47}) values of CO_2 measured with mass spectrometry. *Rapid Commun. Mass Spectrom.*, **30**, 2607–2616.

Searl, A. (1989) Saddle dolomite : a new view of its nature and origin. *Mineral. Mag.*, **53**, 547–555.

Sibley, D.F. and **Gregg, J.M.** (1987) Classification of dolomite rock textures. *J. Sed. Geol.*, **57**, 967–975.

Snell, K.E., **Thrasher, B.L.**, **Eiler, J.M.**, **Koch, P.L.**, **Sloan, L.C.** and **Tabor, N.J.** (2013) Hot summers in the Bighorn Basin during the early Paleogene. *Geology*, **41**, 55–58.

Spötl, C. (1996) Clay minerals as records of temperature conditions and duration of thermal anomalies in the Paris Basin, France. *Clay Min.*, **31**, 203–208.

Stolper, D.A. and **Eiler, J.M.** (2015) The kinetics of solid-state isotope-exchange reactions for clumped isotopes in carbonates: a study of inorganic calcites and apatites from natural and experimental samples. *Am. J. Sci.*, **315**, 363–411.

Stueber, A.M. and **Walter, L.M.** (1994) Glacial recharge and paleohydrologic flow systems in the Illinois Basin: evidence from chemistry of Ordovician carbonate (Galena) formation waters. *Geol. Soc. Am. Bull.*, **106**, 1430–1439.

Swart, P.K., **Cantrell, D.L.**, **Arienzo, M.M.** and **Murray, S.T.** (2016) Evidence for high temperature and ^{18}O-enriched fluids in the Arab-D of the Ghawar Field, Saudi Arabia. *Sedimentology*, **63**, 1739–1752.

Tremolières, P. (1981) Mécanismes de la deformation en zones de plate-frome. Méthode et application au Bassin de Paris. *Rev. Inst. Fr. Pétrol.*, **30**, 743–777.

Tucker, M.E. and **Wright, V.P.** (1990) *Carbonate Sedimentology*. Blackwell, Oxford, 482 pp.

Uriarte, J. (1997) Maturité thermique des sédiments de la bordure sud-est du Bassin de Paris. *PhD thesis, Université de Genève*, 146 pp.

Veizer, J., **Ala, D.**, **Azmy, K.**, **Bruckschen, P.** and **Buhl, D.** (1999) $^{87}Sr/^{86}Sr$, $\delta^{13}C$ and $\delta^{18}O$ evolution of Phanerozoic seawater. *Chem. Geol.*, **161**, 59–88.

Vincent, B., **Emmanuel, L.**, **Houel, P.** and **Loreau, J.-P.** (2007) Geodynamic control on carbonate diagenesis: petrographic and isotopic investigation of the Upper Jurassic formations of the Paris Basin (France). *Sediment. Geol.*, **197**, 267–289.

Violette, S., **Collin, P.Y.**, **Lagneau, V.**, **Aubertin, F.**, **Makhloufi, Y.**, **Charton, R.** and **Bergerat, F.** (2016) Reactive transport modelling of carbonate cementation in a deep saline aquifer, the Middle Jurassic Oolithe Blanche Formation, Paris Basin, France. *Comptes Rendus Geosci.*, **348**, 540–549.

Wang, Z., **Schauble, E.A.** and **Eiler, J.M.** (2004) Equilibrium thermodynamics of multiply substituted isotopologues of molecular gases. *Geochim. Cosmochim. Acta*, **68**, 4779–4797.

Wei, H.F., **Ledoux, E.** and **De Marsily, G.** (1990) Regional modelling of groundwater flow and salt and environmental tracer transport in deep aquifers in the Paris Basin. *J. Hydrol.*, **120**, 341–358.

Wilson, T.P. and **Long, D.T.** (1993) Geochemistry and isotope chemistry of CaNaCl brines in Silurian strata, Michigan Basin, U.S.A. *Appl. Geochem.*, **8**, 507–524.

Worden, R.H. and **Matray, J.M.** (1995) Cross formational flow in the Paris Basin. *Basin Res.*, **7**, 53–66.

Worden, R.H., **Coleman, M.L.** and **Matray, J.M.** (1999) Basin scale evolution of formation waters: a diagenetic and formation water study of the Triassic Chaunoy Formation, Paris Basin. *Geochim. Cosmochim. Acta*, **63**, 2513–2528.

Worden, R.H., **Benshatwan, M.S.**, **Potts, G.J.** and **Elgarmadi, S.M.** (2016) Basin-scale fluid movement patterns revealed by veins: Wessex Basin, UK. *Geofluids*, **16**, 149–174.

Ziegler, P.A. (1990) Geological Atlas of Western and central Europe. In: Shell International Petroleum, 2nd Ed. *Geological Society, London*, Bath, 239 pp.

Manuscript received 26 July 2017; revision accepted 11 October 2017